EARLY-STAGE BREAST CARCINOMA MECHANICALLY REMODELS THE TUMOR MICROENVIRONMENT TO PROMOTE CANCER PROGRESSION

by

Nicholas Yam

A thesis submitted to Johns Hopkins University in conformity with the requirements for the degree of Master of Science and Engineering in Biomedical Engineering

Baltimore, Maryland
May 2018

Abstract

The remodeling of the tumor microenvironment is a characteristic behavior that malignant tumors utilize to progress towards late stages of cancer. Though this has been observed in *in vivo* studies, the measurement of tumor microenvironment remodeling in real-time and the characterization of remodeling events have not been fully studied. Here, we present an *in vitro* platform that can be used in concert with high-resolution confocal microscopy to capture real-time remodeling events in breast carcinoma cell lines of increasing malignancy. We carefully selected three mouse epithelial breast cell lines: EpH4-EV (normal, control), 67NR (non-metastatic, early-stage), and 4T1 (metastatic, stage IV). By embedding 3D cell cultures (spheroids) into a fabricated tumor microenvironment consisting of normal fibroblasts and rat tail type-1 collagen, extracellular matrix (ECM) remodeling was quantified in terms of collagen realignment and pore generation. Other techniques, such as traction force microscopy and fluorescence recovery after photobleaching, were employed to quantify traction stress and diffusion anisotropy due to collagen realignment. Our work demonstrates the significant remodeling events of the early-stage cancer cell line, 67NR, when compared to the control, EpH4-EV. This is quantified in terms of collagen alignment and the generation of collagen pores over time. Along with this remodeling, 67NR generates a diffusion anisotropy as molecules have directed diffusion along radially aligned collagen channels. Moreover, traction stress generation by 67NR spheroids is significantly greater than EpH4-EV, thus connecting force generation to the grade of collagen remodeling. Furthermore, culturing normal fibroblasts in the surrounding ECM results in significantly greater ECM remodeling by the embedded 67NR spheroids, suggesting that mechanical

and chemical cues cause normal fibroblasts to transform into cancer-associated fibroblasts. Additionally, fibroblasts are observed to migrate towards 67NR spheroids. This result is the opposite of what occurs in previous studies, where cancer-associated fibroblasts direct metastasis by attracting cancer cells away from the primary tumor. In conclusion, early-stage, non-metastatic cancer (67NR) utilizes mechanical forces to remodel its surrounding tumor microenvironment to aid in cancer progression.

Advisor: Yun Chen

Readers: Nicholas Durr and Xingde Li

Acknowledgements

To begin with, I would like to thank my research advisor and mentor, Dr. Yun Chen. Thank you for your input and guidance on this extremely difficult project. Next, thank you to Debonil Maity. Without your help throughout the early stages of the project and your help on experiments, I doubt this project would be nearly as complete as it is today. Additionally, I want to thank Wei-Hung Jung and Matthew Pittman for your invaluable input on my project. I am truly blessed to have had the opportunity to work with all of you. Lastly, I want give special thanks to my family, especially my parents and siblings, and friends for supporting me throughout my time here at Johns Hopkins.

Table of Contents

List of Figures

Introduction

Background

Breast cancer results in 30% of all new cancer cases and is the second leading cause of cancer deaths in women[1]. Furthermore, previous research has shown that high breast tissue density is a significant risk factor (1.8- to 6.0-fold increase) for the development of breast cancer[2,3]. This can largely be attributed to high collagen density[3]. Originating in the ductal epithelium for most cases, epithelial breast cancer, also known as breast carcinoma, has been shown to interact with its surrounding tumor microenvironment (TME) through mechanical and chemical pathways[4]. Interactions between the malignant breast tumor and its surrounding TME are of particular interest as these pathways ultimately result in increased proliferation, progression, transformation of nonmalignant cells, resistance from the immune system, and, if left untreated, metastasis[4,5].

The extracellular matrix (ECM) is composed of proteins, proteoglycans, and a plethora of other molecules and is a major component of the TME. The ECM's main structural component is type 1 collagen. Breast carcinomas exert mechanical forces that realign collagen fibers to become perpendicular to the tumor boundary (frequently referred to as radial alignment), therefore generating a stiffer environment and facilitating tumor invasion by producing collagen tracts for migration[6–8]. Additionally, breast carcinomas secrete lysyl oxidase (LOX) to crosslink collagen, thus further increasing ECM stiffness[9]. This remodeling explains the stiffness felt through physical palpations when tumors, especially breast carcinomas, are detected in screenings[10]. With a stiffer ECM, mechanosensitive pathways, such as the FAK-Rho-ERK signaling network, are

activated, thus resulting in cancer proliferation, increased invasiveness, and progression[4,11].

Beyond the ECM, other TME components include fibroblasts, immune cells, blood vessels, adipocytes, etc[12]. Of these, fibroblasts have been of research interest as cancerous tumors manage to facilitate the transformation of normal fibroblasts (NFs) to cancer associated fibroblasts (CAFs). Similar to the mechanical remodeling done by tumors, CAFs play a significant role in driving cancer progression[13,14].

Fibroblasts are the most prevalent cells in the TME[12]. Located throughout the human body, fibroblasts are normally activated for wound healing[13]. Arising from quiescent fibroblasts, NFs become activated via external signals, such as hypoxia, chemokines, and cytokines[13]. Of these external signals, transforming growth factor beta (TGF-β) has been frequently observed and utilized to facilitate the transformation to NFs. Once activated, NFs express α-smooth muscle actin (αSMA), thus upregulating contractile properties[13,15,16]. Therefore, NFs are able to mechanically remodel the ECM and subsequently aid in wound contraction[17,18]. Additionally, NFs rapidly proliferate and secrete ECM components and enzymes, such as matrix metalloproteinases (MMPS), to aid in the reconstruction and remodeling of the ECM to repair the wound[13,19].

From the fibroblasts perspective, tumors are viewed as wounds. Coined by H.F. Dvorak as a "wound that never heals," these cancerous tumors initiate a chronic wound healing response that attracts fibroblasts, a response that ultimately drives cancer progression[13,20,21]. Through the secretion of cytokines (particularly TGF-β), exosomes, and other epigenetic cues in the TME, NFs are irreversibly transformed into CAFs[13,19,22–26]. Exosomes are of particular interest as these 40-100 nm vesicles house many

molecules, such as proteins, mRNA, and miRNA, that can aid in tumor progression[24]. For example, secreted exosomes can contain TGF-β, mRNA, or even have TGF-β on its surface, thus causing CAFs to arise[14,27]. CAFs are key players in cancer progression by actively participating in processes such as ECM remodeling, secreting growth factors for tumor proliferation, and even promoting drug and immune resistance[13]. Additionally, due to the mechanical ECM remodeling imposed by cancer cells, CAFs can readily interact with the tumor and direct metastasis by leading cancer cells out from the primary tumor site[28,29].

However, few of the previous studies are focused on mechanical remodeling events that are imposed by cancer cells. These remodeling events can be important as they are a necessary step for tumor progression, especially at early stages[7,8]. Moreover, a randomly aligned ECM functions as a diffusion barrier, thus hindering the tumor's secretory cues from even reaching NFs efficiently and transforming them into CAFs[30]. Therefore, a better understanding of the risk factors surrounding CAF development needs to be further explored. Particularly, mechanical ECM remodeling by breast tumors and its subsequent effect on the diffusion of these biochemical cues that cause CAFs to arise needs to be further characterized.

3D-Biomimetic Platform

To study tumor-stroma interactions, we developed a platform to mimic *in vivo* processes while also allowing for real-time, high-resolution microscopy to capture ECM remodeling. Compared to *in vivo* experiments, this approach can be significantly more cost-effective and can be applied to other cell lines where tumor-stroma interactions are

of particular interest. Moreover, *in vitro* tumor models are becoming more widely used to visualize *in vivo* processes. These *in vitro* tumor platforms can be used to model various aspects of tumor growth and even utilized as platforms for drug screening and other cell-based assays[31–33].

Spheroids, also known as 3D cell cultures, have previously been shown to be ideal for *in vitro* tumor models[31,32]. Compared to 2D cell culturing, spheroids better depict cell functionality *in vivo* as cells interact with one another and their environment in 3D[32,34]. The added dimension results in significant changes in cell response, which were shown to have more physiological relevance[32,34–36]. Of the methods available for producing these spheroids, the hanging drop method was utilized for this study. Though it may not be the most efficient method, it was the most cost-effective method that allowed for easy tuning of spheroid size and produced relatively uniformly-sized spheroids[31].

With the available methods of producing 3D *in vitro* platforms, we sought to design a platform to fit the needs of this study. Specifically, the platform would need to meet the following criteria: 1) model a 3D tumor and its surrounding TME, 2) allow for real-time, high-resolution imaging to monitor ECM remodeling, and 3) able to be used in concert with other techniques, such as fluorescence recovery after photobleaching (FRAP).

With this in mind, we carefully constructed a platform to meet these criteria. As the core structural component of the ECM, type 1 collagen has been frequently utilized to simulate the ECM surrounding the tumor in *in vitro* platforms[32]. Therefore, this study employed type 1 collagen for this platform. With fibroblasts as a main focal point of this study, normal GFP fibroblasts were embedded into the collagen surrounding the

spheroid. The type 1 collagen and GFP fibroblasts constituted the TME. The most challenging criteria was criterion 2, where the platform would need to be designed to have a thin enough collagen layer to allow for high-resolution imaging, but not too thin that the spheroid would come into contact with the glass surface. This is because the stiffness, especially the high stiffness associated with glass, has significant effects on cell behavior as cells are able to sense the stiffness of the substrate they adhere to[37]. After satisfying this criterion, the developed 3D-biomimetic platform allows for the capturing of dynamic, real-time ECM remodeling while also monitoring fibroblast behavior between spheroids of different breast mammary gland epithelial cell lines.

Fluorescence Recovery After Photobleaching (FRAP)

FRAP is a powerful tool for the analysis and quantification of the diffusion rate of fluorescent molecules. This tool is useful for analyzing protein dynamics and drug mobility[38–40]. FRAP is performed by selecting a region of interest (ROI), recording frames before bleaching for the pre-bleach intensity, using a high-power laser to photobleach the molecules inside the ROI, and then recording the frames after bleaching to document the recovery process. As fluorescent molecules diffuse into the ROI after bleaching and replace the photobleached molecules, a recovery curve is generated[40]. With molecules that have intermediate or limited mobility, there is an inability in the exchange of the photobleached and fluorescent molecules[40]. This inability is termed the immobile fraction and is the difference between the pre-bleach and post-bleach plateau[40]. An example of a FRAP curve is shown in Figure 1.

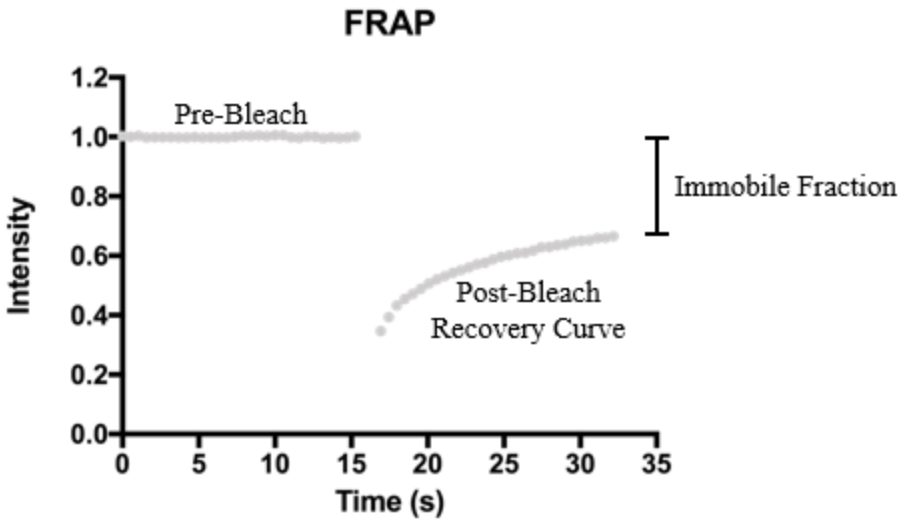

Figure 1. Labeled FRAP curve. This shows the pre-bleach intensity curve, post-bleach recovery curve, and the immobile fraction that can arise when the fluorescent molecules have intermediate or limited mobility.

The recovery curve can be analyzed to obtain the diffusion coefficient of the fluorescence molecules. For this study's purposes, Leica's curve fitting technique was utilized, which fits a single exponential function with one term to the recovery curve[41]:

$$y(t) = F - Ae^{-t/\tau}, \quad (1)$$

where *y(t)* is the fluorescence intensity at time *t*, *F* is the limit value for the recovery curve, *A* is the amplitude of the recovery curve, *t* is the time duration after photobleaching, and τ is the time constant that relates to the diffusion coefficient of the fluorescent molecule.

The diffusion coefficient can then be obtained for a circular ROI using the idealized diffusion model[42]:

$$\tau = \frac{\omega^2}{4*\pi*D}, \quad (2)$$

where ω is the radius of the ROI and D is the diffusion coefficient. Another frequently-utilized method for determine the diffusion coefficient is by using the Soumpasis equation[43]:

$$D = 0.224 * \omega^2 / t_{1/2}, \quad (3)$$

where $t_{1/2}$ ($=ln(2)*\tau$) is the time at which the recovery curve is halfway recovered. From these equations and subsequent experimentation, a relationship between a rectangular ROI and tau has been derived[44]:

$$\tau = (L/2)^2 / (4 * D), \quad (4)$$

where L is the length of the shortest side of the rectangular ROI. With these equations, FRAP can be used to determine if there is indeed a diffusion anisotropy due to collagen alignment.

Traction Force Microscopy

Traction force microscopy (TFM) can be applied to measure the amplitude and directionality of the mechanical forces exerted over an area by cells. The technique begins by preparing substrates of a known elastic modulus with embedded fluorescently-labeled beads. Plating cells on the substrate, the cells are allowed to adhere and spread, followed by generating and transmitting traction forces that causes the deformations of substrate[45]. These deforming forces are generated by the contraction of the actomyosin network, which are then transmitted to the ECM via focal adhesions[45].

The deformed substrate surrounding the cell of interest are imaged first, followed by trypsinization to detach the cell, and then imaged again following cell detachment. After detachment, the traction stress that the cell was exerting onto the substrate is

released, thus causing the substrate and fluorescent beads to relax from its previously deformed state. The movement of the beads from their deformed to relaxed state can then be analyzed to determine the traction stress of the cell onto its substrate.

For the purposes of this study, analysis was performed using a previously established technique[46]. This technique utilizes iterative particle image velocimetry (PIV) to generate a displacement field of the beads. This is done by dividing a pair of images (before and after bead displacement) into several interrogation windows, cross-correlating the images, and generating a displacement field. With this PIV data, the Fourier transform traction cytometry (FTTC) method is used to construct a color coded vector plot of the traction stress[47].

Purpose of Study

One goal of this study is to characterize breast cancer's dynamic ECM remodeling utilizing an *in vitro* 3D tumor model. In particular, the mechanical remodeling that tumors have on its microenvironment needs to be characterized and quantified. Using the platform with and without fibroblasts, it is of pique interest to see differences in ECM remodeling and to see if fibroblast activity varies between normal and cancer cell lines. A second goal is to analyze the diffusion rates, through FRAP, in the remodeled ECM to quantify the effect that remodeling has on the diffusion of small molecules that result in CAF development. The last goal is to quantify the mechanical forces generated by different breast tumors. Traction force microscopy will be used to provide a connection between mechanical force generation and the grade at which the ECM is remodeled.

Ultimately, we hypothesize that early-stage breast cancer overcomes this diffusion barrier by generating greater contractile forces to remodel its TME.

Materials and Methods

Cell Lines

Breast mammary gland epithelial cell lines were selected in order of increasing malignancy. Specifically, the cell lines used in this study are EpH4-EV (normal breast epithelial cells), 67NR (non-metastatic, early-stage carcinoma), and 4T1 (metastatic carcinoma)[48]. These are all mammary gland epithelial cell lines that are of mouse origin.

With regard to fibroblasts, GFP-3T3 fibroblasts were selected because they are frequently used in tumor models to study CAF transformation[49,50]. Moreover, these fibroblasts have green fluorescent protein (GFP), therefore allowing for easy tracking of fibroblast movement over time. This immortalized embryonic cell line is of mouse origin.

2D Cell Culturing

Cell lines were seeded onto cell culture dishes (NEST). These were maintained using a prepared Dulbecco's Modified Eagle Medium (DMEM) containing 10% Fetal Bovine Serum (FBS), and 1% Penicillin Streptomycin (P/S) inside a 37°C and 5% CO_2 incubator (Thermo Electron Corporation). All of the prepared DMEM components were from Thermo Fisher.

Prior to culturing, 0.25% Trypsin-EDTA (referred to as trypsin), Phosphate Buffered Saline (PBS), and prepared DMEM (all from Thermo Fisher) were placed into an incubator to warm up to 37°C. Cells were ready for passaging once 80% confluency

was achieved by checking on a 4x objective of a light microscope (CELENA® S). After removal of the media in the culture dish, cells were washed with 1 mL of PBS. The PBS was then removed and 600 µL of trypsin was added. The dish was then put into the cell incubator for 3 minutes.

After detachment, cells were then pipetted with 1 mL of prepared DMEM to suspend all of the detached cells. Then, 80 µL of the cell solution was transferred into a new plastic dish containing 8 mL DMEM. This dish was then placed into the incubator to grow for approximately 3 days to become confluent again. The remaining cells were either discarded or used for spheroid production.

Spheroid Production

After 2D passaging, the remaining suspended cells in the old plastic dish were placed into a 15 mL conical centrifuge tube. An additional 1 mL DMEM was used to wash the dish and was then added to the conical tube. This was then centrifuged (ELMI CM-6MT) at 1000 rpm for 5 minutes. Following centrifugation, the supernatant was discarded and the cell pellet was suspended in 1 mL DMEM. The cell density was then determined by using 10 µL cell suspension and utilizing an automated cell counter (LUNA™ Automated Cell Counter).

Once the cell density was determined, the appropriate amount of prepared DMEM was added to obtain a cell density of $5*10^4$ cells/40 µL droplet of suspended cells. Using the hanging drop method, a non-cell culture plastic dish was then obtained and filled with 10 mL of PBS to provide a humid environment for the 3D cell cultures. The lid was then flipped over and the 40 µL droplets containing $5*10^4$ cells were placed onto the

underside of the lid with approximately 50 mm separating each droplet. The lid was then carefully flipped back over so the droplets were hanging above the PBS filled dish. This dish was then allowed to incubate approximately 5 days for EpH4-EV cells, 7 days for 67NR cells, and 5 days for 4T1 cells for a spheroid to form.

Once formed, the spheroids were transferred to an ultra-low attachment 96-well plate (Corning) filled with 100 µL of prepared DMEM. The pipette tip used to transfer these spheroids had to be cut so the spheroids would not rupture. These spheroids were then used in 1-4 days for collagen embedding or TFM. Figure 2 shows the hanging drop method that is followed by transferring to 96-well plates.

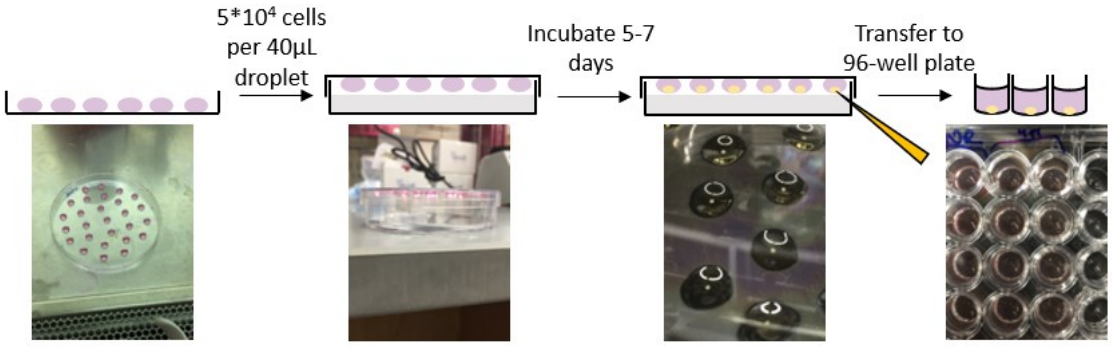

Figure 2. Process of producing spheroids via hanging drop method. Spheroid droplets are carefully flipped over to prevent streaking. The hanging drop dish is then allowed to incubate for a few days before transferring spheroids into a 96-well plate supplied with fresh culture media.

Collagen Preparation

Rat tail type 1 Collagen (Corning) was diluted to a 3 mg/mL concentration using a 3:1 ratio of 10x DMEM and 0.1 M NaOH. The collagen we purchased had a concentration of 3.3 mg/mL. This required 461 µL of collagen, 36.75 µL of 10x DMEM,

and 12.25 µL of 0.1 M NaOH. Whenever pipetting the collagen solution, the pipette tip was cut off and the collagen was gently pipetted. Once the diluted collagen solution was prepared, the solution was slowly pipetted 2 times to mix all of the components together.

Spheroid Embedding

Prior to embedding the spheroid into collagen, 6 wells of a 24-well glass bottom dish with #0 cover slip (Cellvis) were coated with 500 µL of 0.1% (w/v) in H_2O Poly-L-Lysine solution (Sigma-Aldrich). This was allowed to incubate overnight. After incubation, the Poly-L-Lysine solution was removed and washed with 500 µL PBS for 10 minutes. The PBS was then removed and the dish was allowed to air dry.

Once the collagen solution and dish were prepared, 15 µL of collagen was plated onto the dish in a star shaped pattern to prevent drying out of the collagen from the center of the dish. The dish was then covered and allowed to partially gel for 15 minutes or until collagen fibers were visible using the 4x objective on the light microscope. The remaining collagen solution was kept in the 4ºC until needed. When collagen fibers were formed, the spheroid was carefully removed from the 96-well dish and plated on top of the collagen without allowing the pipet tip to touch the collagen gel. The media surrounding the spheroid was then carefully pipetted out. The spheroid was then allowed to adhere to the collagen for 30 minutes while the dish was wrapped in Parafilm M to prevent dehydration of the collagen. This spheroid-collagen platform was then used in either experimentation with (co-culture) or without fibroblasts.

Spheroid and Collagen Without Fibroblasts

After allowing the spheroid to adhere, the collagen solution stored (420 μL) at 4ºC was used to cover the spheroid. To do this, collagen solution (40 μL) was carefully added on top of the spheroid. This was allowed to gel for 2 hours at room temperature. After gelation, 2 mL of prepared DMEM was added into each well. The dish was then allowed to incubate for at least 1 day before imaging was done.

Co-Culture Samples

For this method to work, GFP-3T3 fibroblasts are needed to achieve 80% confluency at the time of spheroid embedding.

While allowing the spheroid to adhere, GFP-3T3 fibroblasts were passaged and the remaining cell solution was centrifuged at 1000 rpm for 3 minutes. The supernatant was then discarded, and the pellet was resuspended in 1 mL of prepared DMEM. A fibroblast concentration of $2*10^5$ cells per spheroid needed to be obtained. Once the appropriate amount of cell suspension needed to achieve this concentration was obtained, the suspension was centrifuged again at the same settings. After discarding the supernatant, the cell pellet was resuspended in 40 μL of prepared DMEM.

Next, assuming there are 6 embedded spheroids, 240 μL of the collagen solution was gently pipetted into the cell suspension. Then, 40 μL of fibroblast-collagen solution was carefully plated on top of the embedded spheroid. This was allowed to gel at room temperature for 2 hours before 2 mL of prepared DMEM was added to each spheroid well. These co-culture dishes were then incubated for at least 1 day before imaging was done.

Confocal Microscopy

Live imaging was performed using an oil immersion, 63x/1.40 (Magnification/Numerical Aperture) objective on Leica's TCS SP8 confocal microscope. An incubation chamber was used to maintain 37ºC, 5% CO_2, and appropriate humidity, conditions of which mimic the incubators used for cell cultures. Samples were imaged for up to 22 hours. Transmitted light was used to monitor the spheroid boundary. Leica's hybrid detector (HyD), a photodetector that combines photomultiplier tubes (PMT) and super-sensitive avalanche photodiodes (APDs), was utilized at a 655 nm wavelength for reflectance imaging to capture scattered light from the collagen fiber remodeling. Additionally, HyD LightGate, which only affects this reflectance channel, was employed. The LightGate removes unwanted signals by measuring the time decay of the signal. This LightGate feature was set from 0 to 4.25 nanoseconds to remove the background noise signal caused by the oil-glass interface. For co-culture samples, the GFP signal of the fibroblasts was captured at excitation and emission wavelengths of 488 nm and 510 nm, respectively, using a second HyD channel that was set at 502-621 nm to capture the fluorescence emission. After imaging, samples were put back into the cell incubator for further testing.

Sample Fixation

Samples were fixed utilizing 4% paraformaldehyde (PFA) in PBS (Affymetrix). To begin with, the media was carefully removed from each well and placed into separate 1.5 mL microcentrifuge tubes. After media removal, 1 mL of the PFA solution was added to each well. This dish was then allowed to incubate at 4ºC for 16 hours. Following, the

PFA solution was removed, and the wells were washed using PBS in steps of 10, 20, and 30 minutes before storing in 1 mL of PBS for FRAP experiments and future experiments. The microcentrifuge tubes were then frozen at -20ºC for future analysis experiments.

Fluorescence Recovery After Photobleaching

FRAP was conducted using fluorescein isothiocyanate (FITC) 2000 kDa dextran (SigmaAldrich). The FITC 2000 kDa dextran was selected as a test molecule to study diffusion in the TME since its diameter (54 nm) falls within the size range (40-100 nm) of exosomes[24,51]. To begin with, the FITC-dextran was dissolved by PBS to obtain a final concentration of 10 mg/mL. PBS was used since its pH of 7.4 corresponds to dextran's highest fluorescence intensity[51]. The samples were allowed to warm up to 37ºC for at least 30 minutes in the cell culture incubator prior to FRAP in a pre-warmed Leica TCS SP8 confocal microscope incubator that was equipped with the FRAP booster module.

For bleaching, an argon laser was set at 95% power (190 mW) in Leica's software. For the pre- and post-bleaching frames, the white light laser was set at 0.1% power (0.05 mW) to minimize photobleaching. To image the FITC-dextran, excitation and emission was set at 490 nm and 520 nm, respectively, using a PMT channel that was set at 510-530 nm to capture the fluorescence emission. The collagen imaging was done using the reflectance settings as mentioned earlier, but on a PMT channel without LightGate. Samples were then bleached using rectangular FRAP (rFRAP), where a ROI was first drawn normal to the spheroid and then another ROI was drawn perpendicular to the first ROI on regions of high collagen density and alignment. These ROIs were 60 μm by 10 μm (Figure 3). This was all done using 30 pre-bleach frames, 2 bleaching frames,

and 30 post-bleach frames at 0.525 seconds per frame (512x512 pixels, 1000 Hz scanning speed, and bidirectional mode). Recovery curve data was then saved, particularly the τ value.

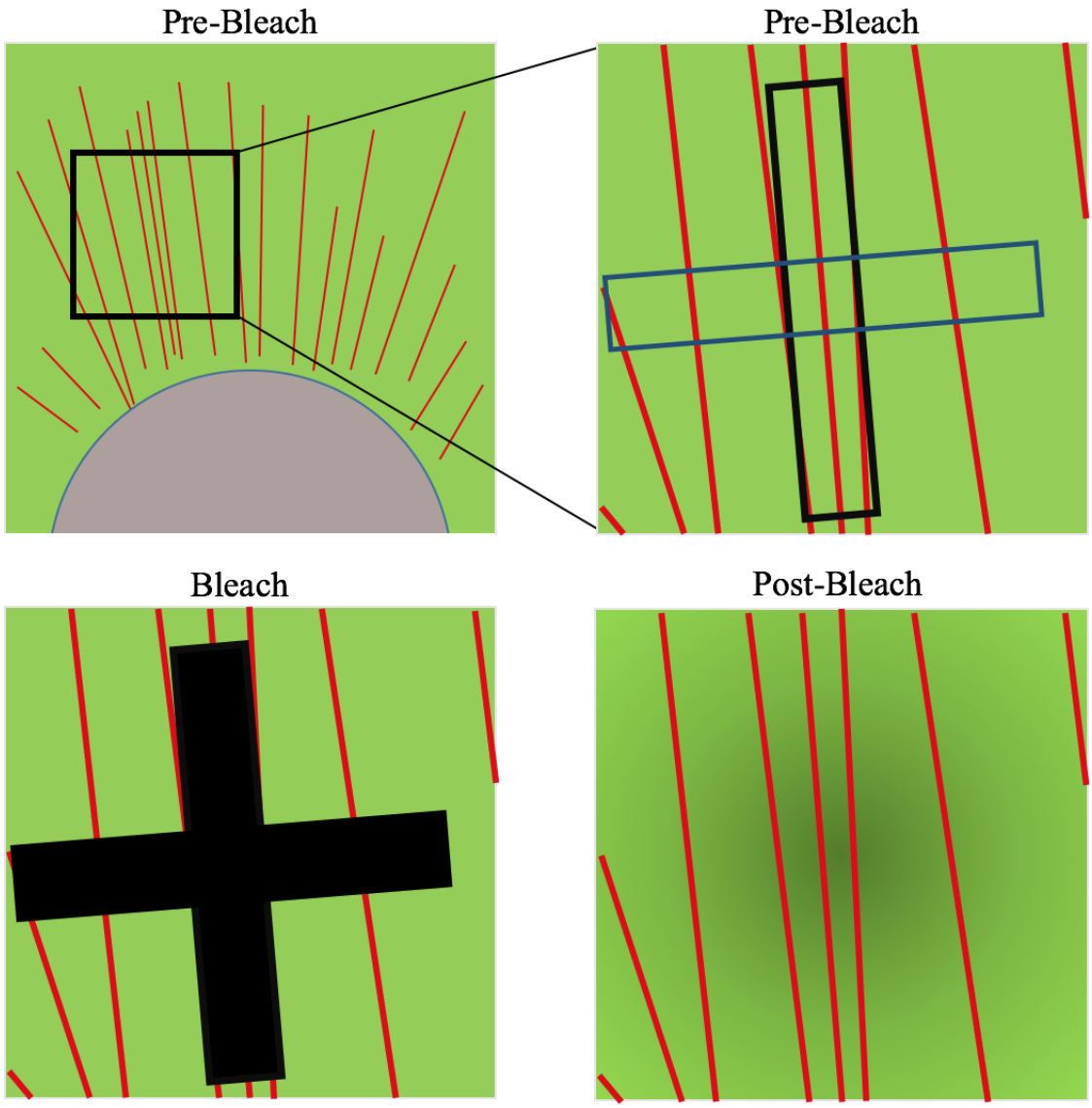

Figure 3. FRAP schematic illustrating ROI orientation along with pre-bleach, bleach, and post-bleach examples. The FITC-dextran constitutes the green background. Two ROIs, one oriented along collagen (red) towards spheroid (black) and the other perpendicular to that ROI (blue), are placed in a region of aligned, dense collagen. This ROI is then

bleached and then allowed to recover. The post-bleach intensity gradient is due to the immobile fraction that is present following bleaching.

Traction Force Microscopy

Traction force microscopy utilizes a soft substrate made of silicone gel (CY 52-276 A:B = 1:1 ratio, Corning). This soft substrate was prepared at room temperature, plated onto wells of a 24-well #0 cover slip dish (40 µL per well), and allowed to gel overnight at room temperature. At the ratio of preparation utilized, the soft gel had an elastic modulus of 3 kPa[52]. Then, FluoSpheres™ 0.1 µm diameter red carboxylate-modified beads (Thermo Fisher) were prepared at a 1:25000 dilution in PBS. This bead solution was ultrasonicated with ice packs for 1 hour. Afterwards, 100 µg/mL of 1-ethyl-3-(3-dimethylaminopropyl)carbodiimide hydrochloride (EDC, Thermo Fisher) was added to the bead solution. The substrate was then coated in 500 µL of 2% (3-Aminopropyl)triethoxysilane (APTS, Sigma-Aldrich) that was diluted in PBS. The APTS solution was left on the substrate for 5 minutes and then removed. Finally, 500 µL of bead solution was added onto the substrate and allowed to adhere for 2 hours at room temperature.

Once embedded with beads, the bead solution was removed, and 1 mL of PBS was added to immerse and wash the substrate. This washing step was done for 1 hour at room temperature. The substrate was then coated with a 200 µg/mL of rat tail type 1 collagen and 100 µg/mL of EDC in PBS. This was kept for 1 hour at 37ºC in the incubator. This solution was then removed. The spheroid was then added and allowed to attach for 1 hour before 1 mL of prepared DMEM was added. Then, the spheroid was

kept at 37ºC in the incubator for 41 hours to allow for the deformation of the substrate. Finally, TFM was conducted on the Leica SP8 confocal microscope using a water immersion 40x/1.2 objective.

For TFM, the beads were imaged using a PMT channel set at excitation and emission wavelengths of 580 nm and 595-615 nm, respectively. To image the spheroid, the PMT transmitted light channel was utilized. To obtain frames for analysis, one frame was acquired before spheroid detachment. Then, 1 mL of trypsin was carefully added to the spheroid and allowed to incubate for 30 minutes before flushing out the spheroid by using the pipette. Once detached, another frame was captured. These two frames are shown in Figure 4.

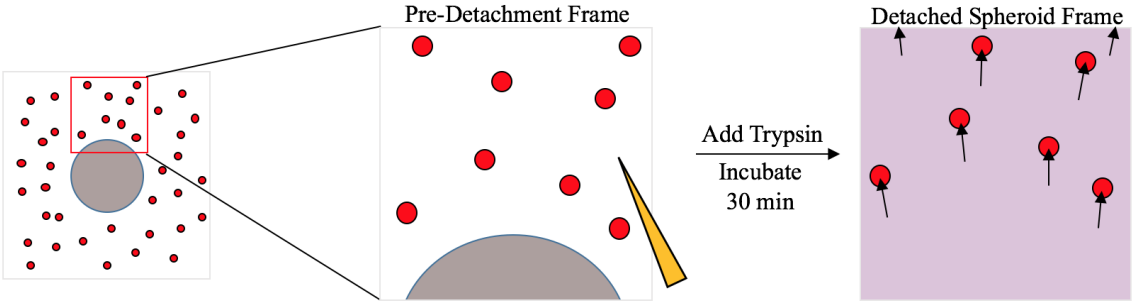

Figure 4. TFM schematic showing the trypsinization of the spheroid and movement of the fluorescent beads after spheroid detachment and substrate relaxation. The spheroid and its surrounding fluorescent beads are first imaged. The spheroid is then incubated with trypsin for 30 minutes to allow for spheroid detachment. Once detached, the substrate relaxes and beads return back to their pre-substrate deformation positions.

The bead displacement between the two frames was then analyzed utilizing ImageJ plugins based on the previously established protocol[46,47]. This analysis is done by generating an image stack with the detached spheroid frame being the first slice and the

attached spheroid frame being the second slice. Then, the PIV plugin was used to generate a displacement field of the beads. Next, the FTTC plugin was used to reconstruct a color coded vector plot of the traction stress[47].

Image, Data, and Statistical Analysis

Images were processed and analyzed utilizing ImageJ. For directionality analysis, a ROI that was 36.06 μm by 36.06 μm was used to define set distances that were 65, 130, and 195 μm away (confirmed by drawing a line) from the spheroid boundary. At these distances, the directionality plugin was used and the dispersion (standard deviation) was recorded. The directionality plugin analyzes the collagen fiber orientation through Fourier components analysis and generates a histogram that shows the orientation of these fibers. The histogram is fitted by a Gaussian function that gives the direction (in º) at the center of the Gaussian, the goodness of fit, and the dispersion (in º) of the Gaussian. For porosity analysis, mean thresholding was utilized on reflectance images to remove background noise. Then, everything besides the spheroid was included in a drawn ROI. Finally, the first and last reflectance images were measured for % area. The porosity change was calculated by doing the percent difference between the two measurements.

For FRAP data, intensity measurements were corrected with respect to pre-bleaching frames using MATLAB's curve fitting application. With this application, a custom curve fitting equation was applied:

$$y(t) = Ae^{-Bx} + C, \tag{5}$$

where *y(t)* is the fluorescence intensity, *x* is time in seconds, and *A*, *B*, and *C* are unitless coefficients. The coefficients were extracted from the curve fitting and was used to

normalize (using Eq. 5) all intensity measurements for the ROI of interest. The corrected intensity data over time was then extracted. This corrected data was then utilized to generate FRAP graphs. Moreover, the tau from each FRAP ROI was averaged and the standard error of the mean was calculated. For TFM, analysis and stress map generation were done utilizing the TFM ImageJ plugins as previously described[46,47].

For the production of graphs and statistical analysis (student t-test), Prism 6 software was used. For the data collected, the mean and standard error of the mean were determined and plotted accordingly. Figures and schematics were constructed using PowerPoint 2016.

Results and Discussion

Spheroids Fabrication

Spheroids are approximately 492.0 ± 14.2 μm (N = 18, where N is the number of samples) in diameter. We observed that 67NR spheroids took the longest to form and many of the spheroids had to be removed due to improper spheroid formation. This can likely be attributed to E-cadherin expression, a cell adhesion molecule that plays a role in forming cell-cell junctions, in EpH4-EV and 4T1 cell lines and lacking in 67NR[6,53]. Though lacking in E-cadherin, 67NR does express N-cadherin, which also functions in cell-cell adhesions[53].

67NR Significantly Remodels its ECM

Without fibroblasts, we observed that the three cell lines show markedly different spheroid-ECM interactions. The interactions are expected and correspond to the

malignancy of the cell line. Ranging from little ECM remodeling to rapid metastasis, these events are captured in the confocal images shown in Figure 5 to highlight the tumor boundary and cell migration over time and Figure 6 to show the reflectance imaging of the collagen fibers being remodeled over time.

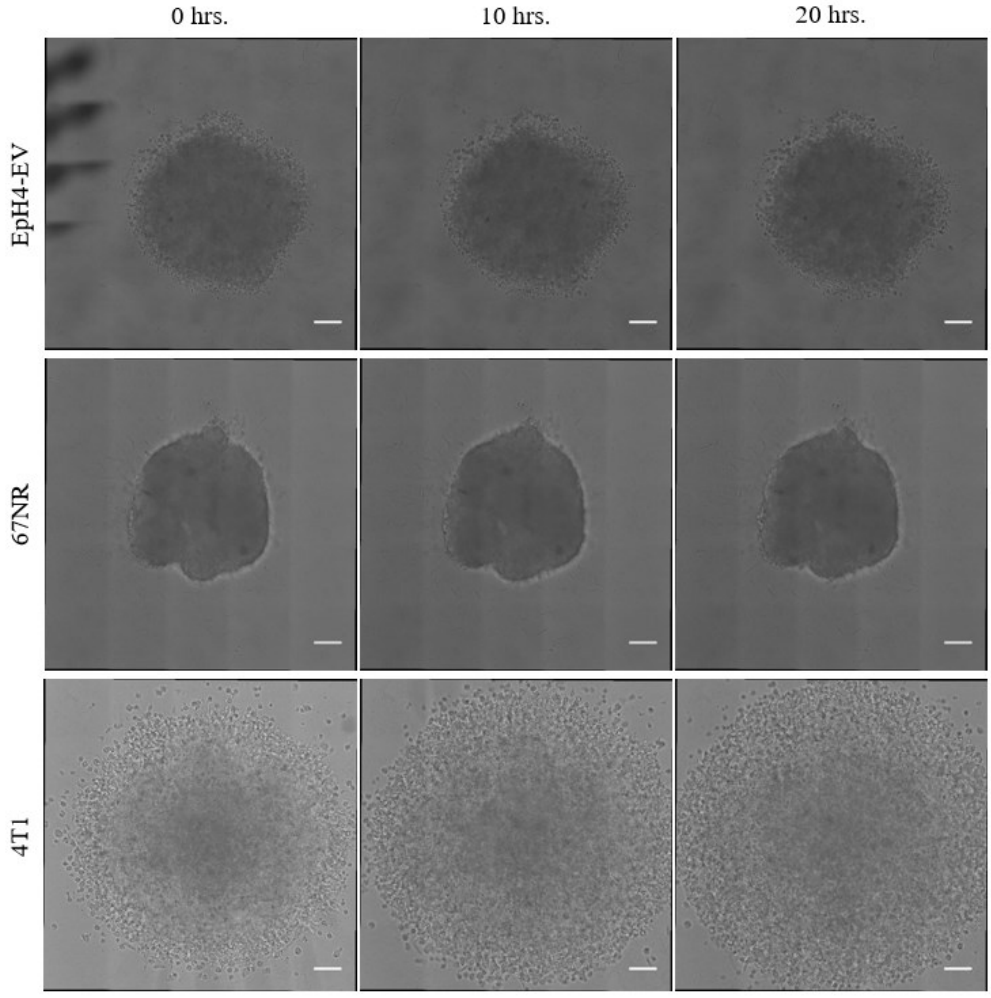

Figure 5. Transmitted light images of all three cell lines over a 20-hour imaging session to show spheroid boundary. EpH4-EV and 67NR has little change in tumor boundary. 4T1 has no boundary at the start of imaging and rapidly metastasizes. Scale bar is 100 μm.

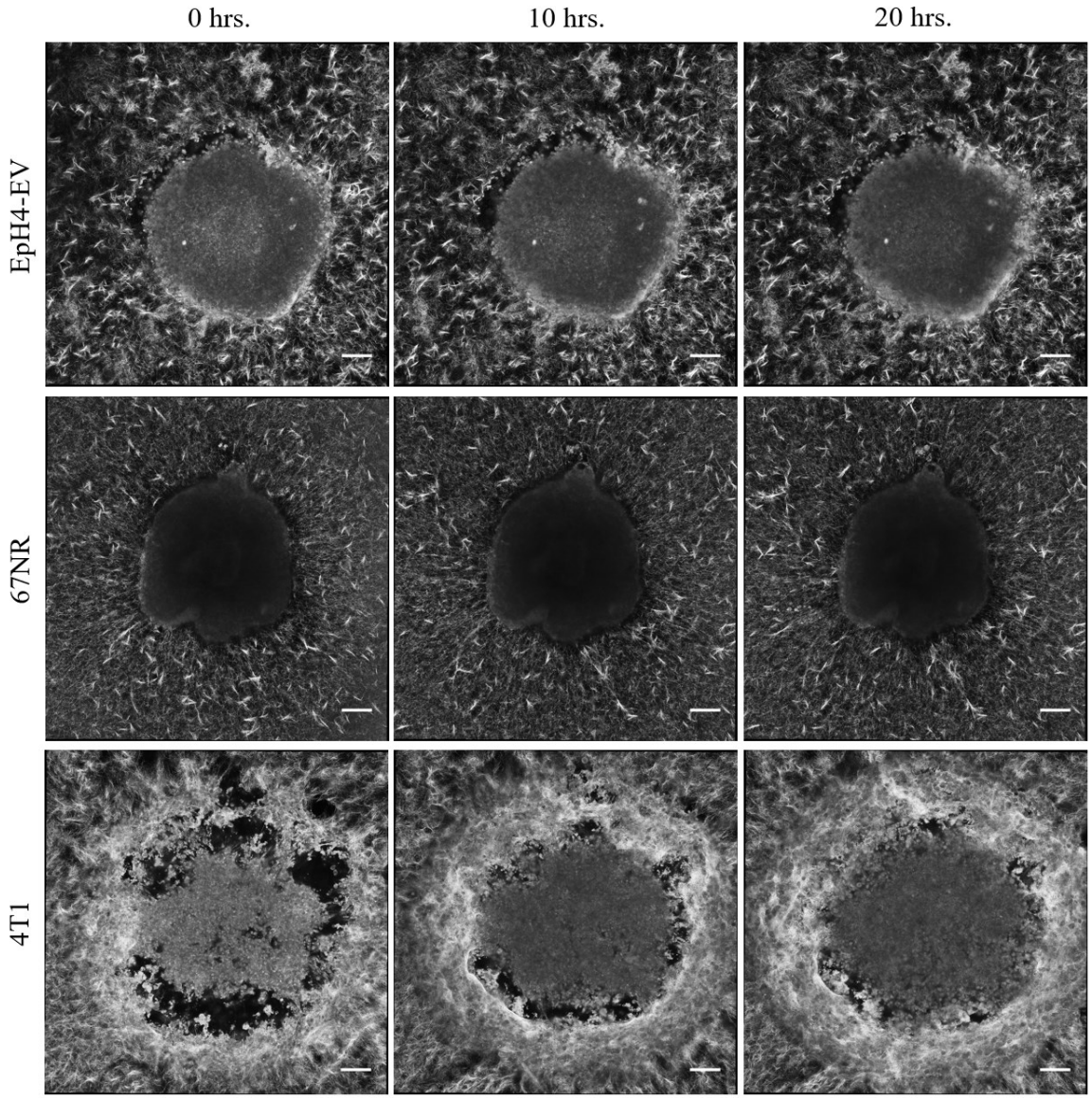

Figure 6. Reflectance imaging of all three cell lines over a 20-hour imaging session to show collagen fiber remodeling over time. EpH4-EV has very little collagen remodeling as fibers are randomly aligned. 67NR has significantly more remodeling as fibers become normal to the spheroid boundary. 4T1 rapidly metastasizes into the surrounding collagen. Scale bar is for 100 μm.

Unsurprisingly, 4T1 spheroids, rapidly disintegrate and migrate into the surrounding ECM over time (Figure 6), a characteristic attributed to its high metastatic potential that mimics stage IV breast cancer in humans[48,54]. Therefore, due to its metastatic behavior and rapid invasion and remodeling of the ECM, subsequent analysis and experimentation of 4T1 samples are discontinued as its collagen alignment and porosity are unquantifiable.

Comparing the normal and early-stage cancer cell lines, 67NR consistently remodels its ECM into aligned collagen fibers when compared to EpH4-EV. This difference is qualitatively illustrated in Figure 7.

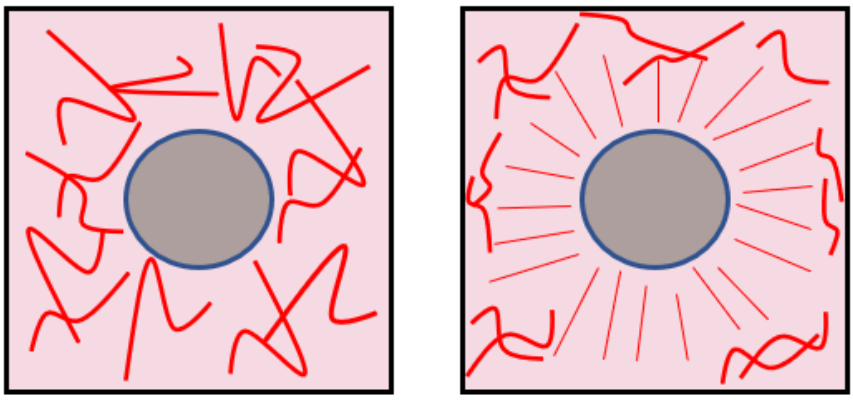

Figure 7. Schematic representing anisotropic (left) and radial (right) collagen realignment. The radial collagen alignment falls off after a certain distance and becomes anisotropic alignment.

To overcome the anisotropic collagen alignment, 67NR spheroids are observed to exert significant mechanical, contractile forces over time to realign the collagen fibers. In comparison, EpH4-EV spheroids are not able to remodel the collagen fibers as

effectively. This collagen remodeling can be clearly seen in Figure 8. Additionally, the contractile behavior of the spheroid can be visualized in Figure 9.

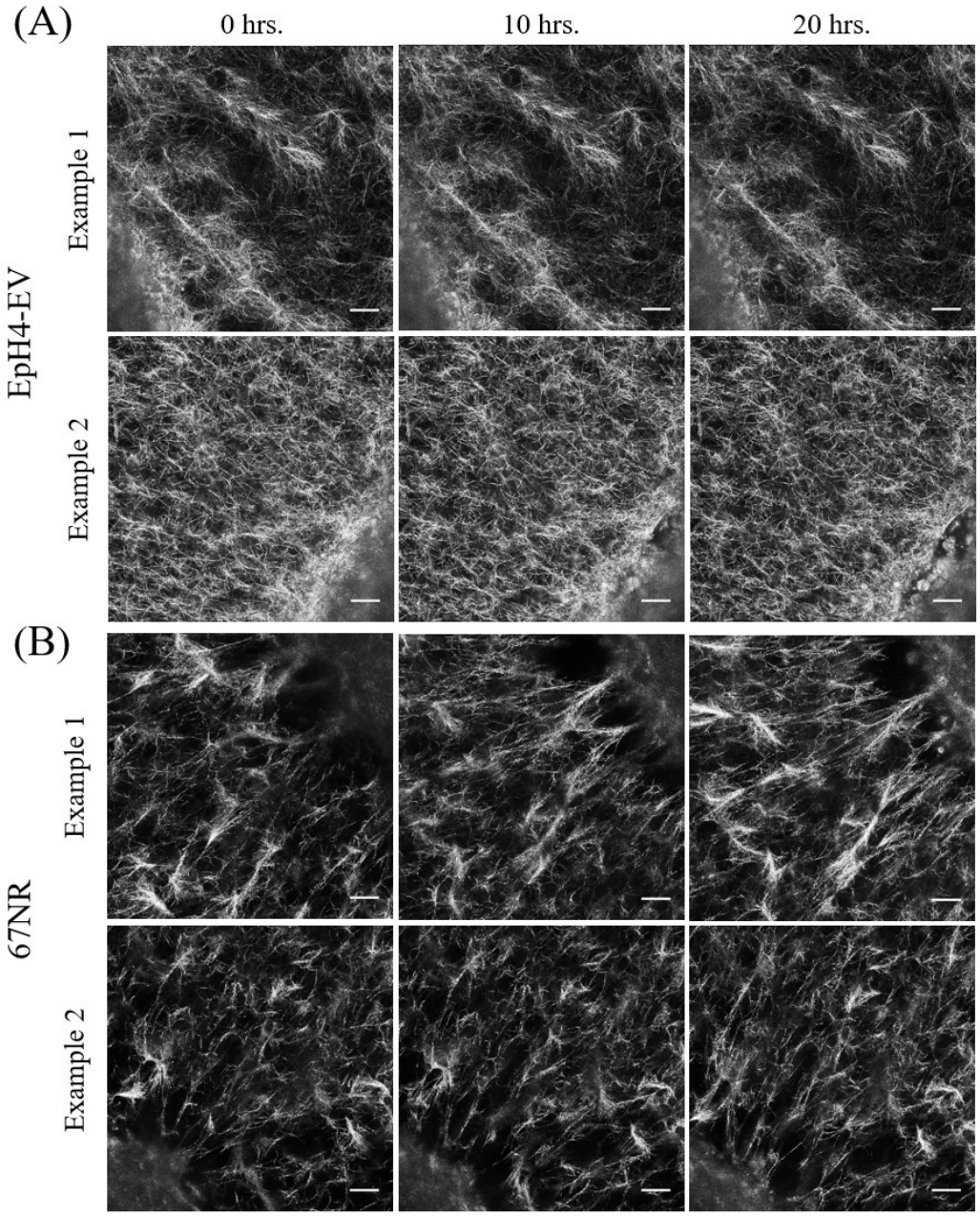

Figure 8. Reflectance imaging of **(A)** EpH4-EV and **(B)** 67NR spheroid-ECM interactions. For **(A),** EpH4-EV has very little collagen remodeling in Example 1. For Example 2, EpH4-EV has some contractile properties as some fibers close to spheroid are

radially aligned. For **(B)**, Example 1 and 2 show significant mechanical remodeling of ECM over time as fibers become radially aligned. Scale bar is for 25 μm.

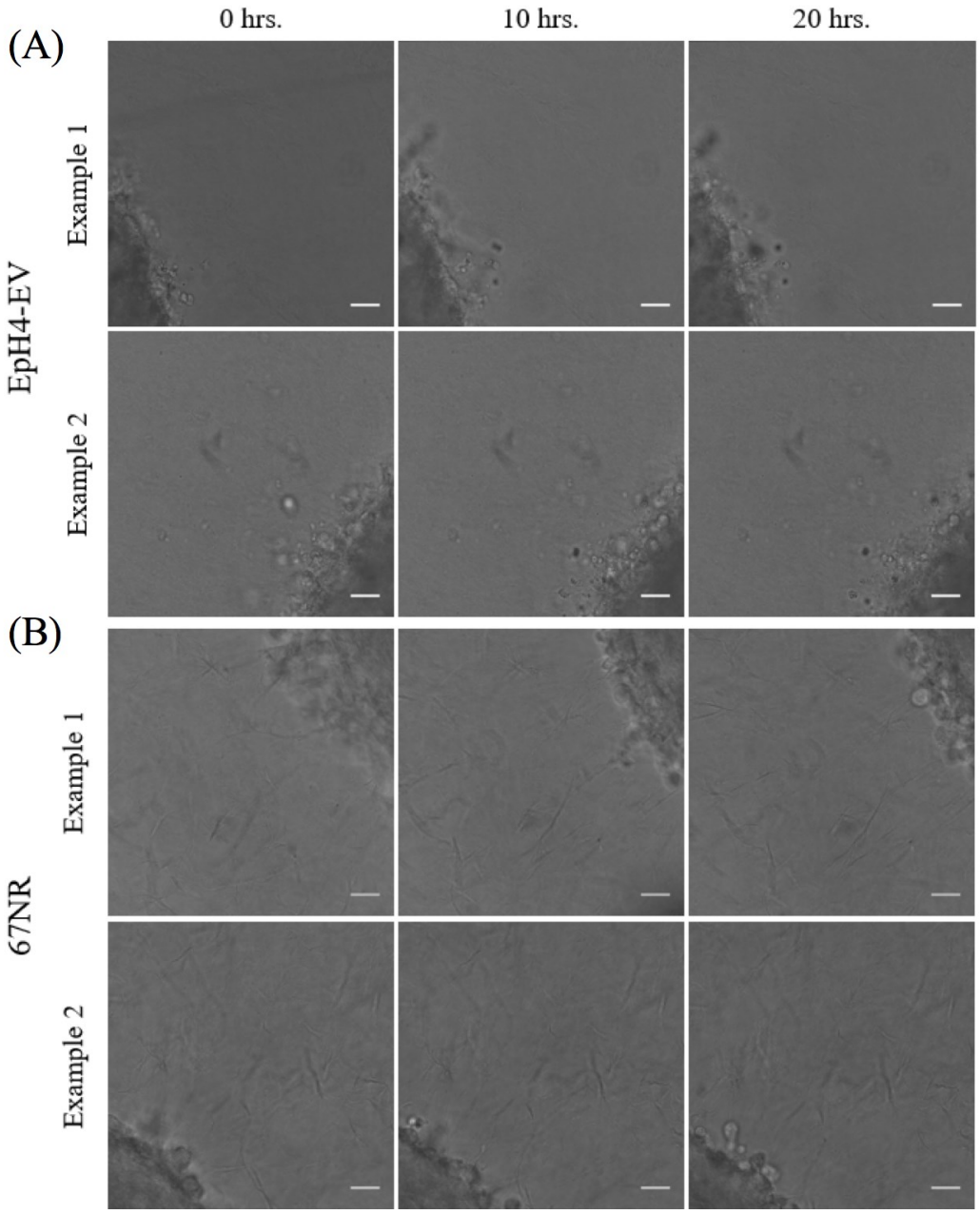

Figure 9. Spheroid boundary of **(A)** EpH4-EV and **(B)** 67NR spheroids as a function of time, all of which correspond to the examples in Figure 8. For **(A)**, EpH4-EV spheroid boundary remains in place in Example 1. For Example 2, EpH4-EV spheroid boundary

recedes over time due to contractile behavior. For **(B)**, both 67NR spheroids contract over time as the spheroid boundary recedes into its respective corner. Scale bar is for 25 μm.

67NR spheroids showed bulk contraction over time, resulting in 67NR spheroids appearing to slowly move out of the frame over the time points shown in Figure 8(B) and 9(B). In comparison, some EpH4-EV spheroids do exhibit contractile properties, but not at the same scale comparable to 67NR. Even with contractile properties, EpH4-EV spheroids are not capable of remodeling its surrounding ECM as extensively.

Along with collagen realignment, the contractile forces being generated by spheroids were also capable of generating pores in the collagen network. The collagen realignment and porosity of the EpH4-EV and 67NR samples are quantified below.

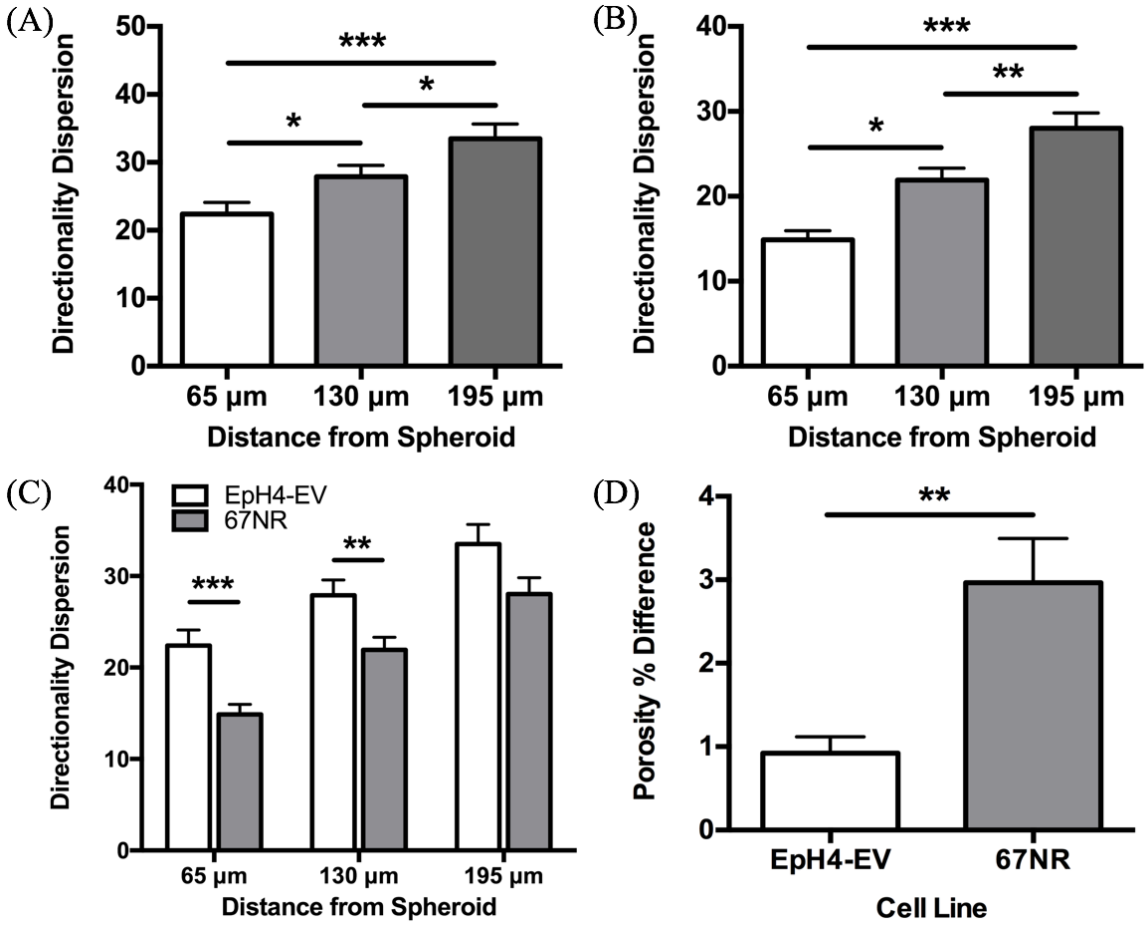

Figure 10. Directionality and porosity analysis of samples without fibroblasts. Directionality dispersion as a function of distance of **(A)** EpH4-EV, **(B)** 67NR, and **(C)** EpH4-EV vs 67NR. **(D)** Porosity between EpH4-EV and 67NR. Higher collagen alignment and pore generation in 67NR spheroids is observed. *p-value < 0.05, **p-value < 0.01, and ***p-value < 0.001. N = 5.

Higher directionality dispersion means that collagen alignment is random and anisotropic. Over these measured distances, Figure 10(A) supports the visual observations obtained in Figures 6 and 8(A) where directionality dispersion is 22.4 ± 1.65, 27.9 ± 1.64, and 33.5 ± 2.10 for 65, 130, and 195 µm distances, respectively.

Though there is some collagen alignment close to the EpH4-EV spheroids at 65 μm, this alignment rapidly and significantly falls off at 130 μm and 195 μm into anisotropic collagen alignment. In comparison, Figure 10(B) shows that 67NR spheroids have dispersions of 14.9 ± 1.06, 21.9 ± 1.36, and 28.0 ± 1.76 for 65, 130, and 195 μm, respectively. As can be seen, 67NR is able to more effectively remodel and radially align its surrounding collagen fibers. Comparing the directionality of the two cell lines in Figure 10(C), it is clear that 67NR significantly remodels its ECM more than EpH4-EV at the 65 and 130 μm distances. Finally, porosity analysis in Figure 10(D) showed significantly larger pore generation in 67NR spheroids (2.97 ± 0.504) in comparison to EpH4-EV spheroids (0.921 ± 0.184). All of these results are likely attributed to higher force generation by 67NR spheroids.

Though 67NR is a non-metastatic cell line, these spheroids effectively remodel its ECM utilizing mechanical forces to generate a stiffer, radially-aligned environment, similar to what occurs *in vivo*[6–8]. This is characteristic of tumor progression as the tumor is preparing to invade the ECM[7]. Additionally, the radial alignment and pore generation in the collagen network can help in the diffusion of cytokines and exosomes.

Diffusion Anisotropy from FRAP

FRAP experiments reveal diffusion anisotropy that the collagen fibers impose. An example of a FRAP session is shown in Figure 11.

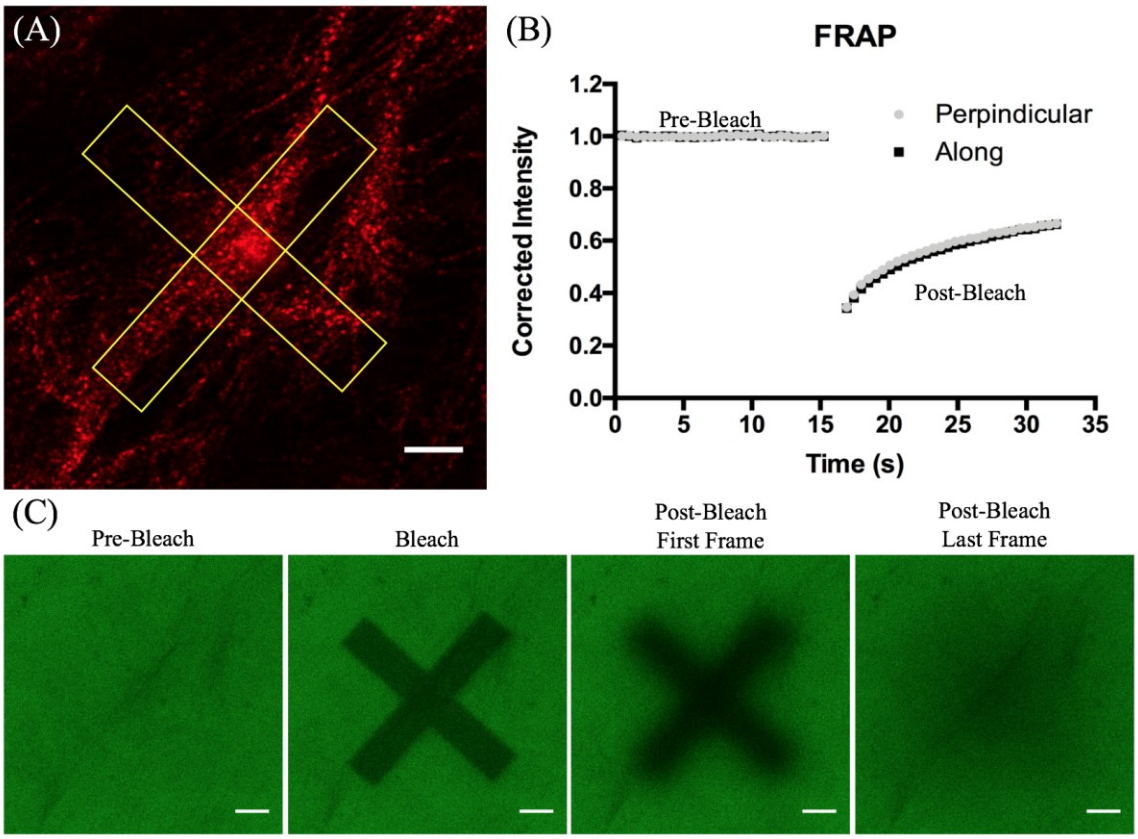

Figure 11. FRAP along and perpendicular to collagen fibers. **(A)** Example of ROI (yellow) selection along and against collagen fibers (red). **(B)** Pre-bleach and post-bleach curve showing corrected intensity as a function of time for the ROI along and perpendicular to the collagen fiber. **(C)** Pre-bleach, bleach, and post-bleach frames corresponding to the graph where FITC-dextran is in green. Scale bar is for 25 μm.

With the pre-bleach, bleach, and post-bleach frames set at 30, 2, and 30 frames, respectively, recovery curves are obtained. Though the recovery curve never truly plateaus, experiments utilizing longer post-bleaching frames had shown incremental intensity recovery towards pre-bleaching levels since the FITC-dextran is not bound to anything. The diffusion anisotropy is quantified in Figure 12.

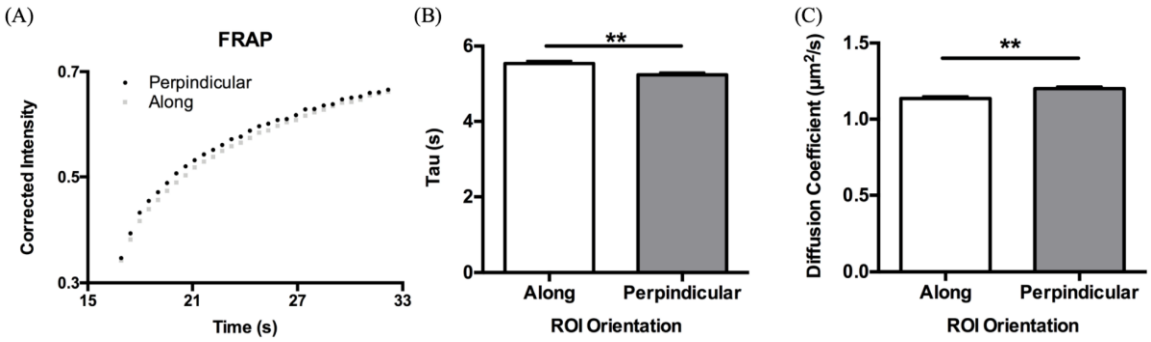

Figure 12. FRAP diffusion anisotropy graphs of **(A)** corrected recovery curve, **(B)** tau (τ) values and **(C)** diffusion coefficients of ROIs that are along and perpendicular to the aligned collagen. Recovery curves are seen to be faster for perpendicular ROIs, therefore resulting in lower τ value. Perpendicular diffusion coefficients are also consistently higher than the diffusion coefficients along the collagen fibers. **p-value < 0.01. N = 5.

Though the overall FITC-dextran diffusion coefficient remains constant, there is a diffusion anisotropy due to collagen alignment[55]. As can be seen from Figure 12(A), there is a difference in recovery curves for the two ROIs used, where the perpendicular ROI (p-ROI) recovers faster than the along ROI (a-ROI). Visualized in Figure 12(B), a τ value of 5.54 ± 0.0688 seconds and 5.24 ± 0.0614 seconds for a- and p-ROIs, respectively, are obtained. This is a 5.54% decrease in τ value from the a-ROI to the p-ROI. These differences in recovery likely arise because the aligned collagen forms channels that prevents the diffusion of FITC-dextran across fibers. Therefore, for the a-ROI the recovery curves have a higher τ (slower recovery (Figure 12(A)) because diffusion of the FITC-dextran is confined within the collagen channels, and the ROI is 60 μm along the length of the collagen channel. In comparison, p-ROI recovery curves have a higher τ (faster recovery (Figure 12(A)) because only a 10 μm bleached length needs to

be filled inside of the collagen channels. Essentially, FITC-dextran molecules need to diffuse 30 μm and 5 μm distances to get to the midpoint of the a- and p-ROI, respectively, due to confinement within collagen channels. Additionally, p-ROIs extend into more porous regions where diffusion is unimpeded by collagen networks.

Equation 3 is then utilized to determine the diffusion coefficient corresponding to the fitted recovery curve and τ value. As can be seen in Figure 12(C), diffusion coefficients have a significant difference as 1.14 ± 0.0568 $\mu m^2/s$ and 1.20 ± 0.0144 $\mu m^2/s$ are calculated for a- and p- ROIs, respectively. This is a 5.26% increase in diffusion coefficient from a-ROI to p-ROI. These data confirm the diffusion anisotropy due to collagen alignment. This diffusion anisotropy that has arisen due to collagen alignment has been shown elsewhere utilizing mathematical models, where increasing collagen alignment resulted in greater diffusion anisotropy[55].

The diffusion anisotropy due to radially aligned collagen reveals the significance of collagen realignment. The alignment effectively overcomes the diffusion barrier, thus promoting CAF transformation because growth factors and exosomes are able have more directional diffusion along collagen channels down a concentration gradient (as opposed to the undirected, impeded diffusion in randomly aligned collagen networks). With this aligned collagen, CAFs are likely to be able to develop from NFs, thus allowing for CAFs to aid in cancer progression.

67NR Generates Significant Traction Stress

Through TFM, it is shown that 67NR spheroids generate significantly more traction stress when compared to EpH4-EV spheroids, as shown in Figure 13.

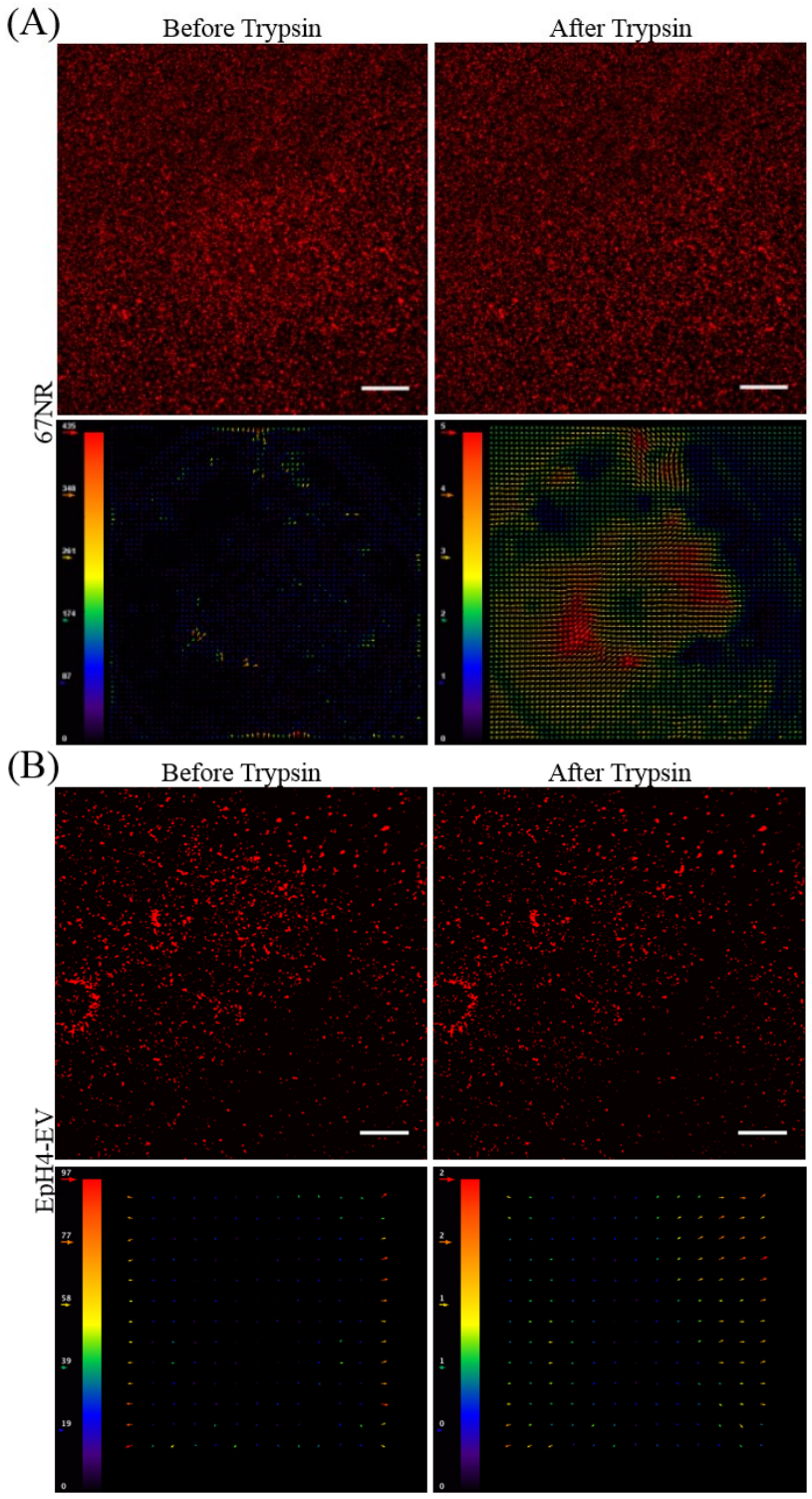

Figure 13. TFM for a **(A)** 67NR and **(B)** EpH4-EV samples. For **(A)**, 67NR shows traction stress release after trypsinization and removal of the spheroid. The bottom left image shows the traction stress map with units of Pascal for the color bar. The bottom

right image shows the displacement in pixels of the beads with units of pixels for the color bar. This traction stress is approximately 435 Pa. For **(B)**, EpH4-EV had no traction stress release after trypsinization. The traction stress map (approximately 97 Pa) and displacement of pixels is due to noise that appeared between the two frames. EpH4-EV has larger interrogation windows for analysis to account for this noise. Scale bar is for 100 μm. N = 2.

Experiments show that EpH4-EV spheroids are not as capable of generating traction stresses as 67NR spheroids. 67NR spheroids are capable of generating up to 435 Pa of traction stress (Figure 13(A)). The 97 Pa of traction stress that is observed for EpH4-EV in Figure 13(B) is due to noise that appears before and after trypsinization of the spheroid.

These observations agree with the mechanical ECM remodeling capacity exhibited in Figures 6 and 8. Moreover, 67NR's ability of generating greater traction stresses are likely to directly contribute to the extensive ECM remodeling, implying a plausible mechanism of tumor progression at early stages; through radial collagen alignment and subsequent stiffening of the ECM, these tumor-ECM interactions ultimately drive further cancer development towards metastasis.

67NR Significantly Remodels its TME

With the inclusion of a significant component of the TME, fibroblasts, 67NR spheroids exhibit amplified remodeling behavior when compared to their non-co-cultured counterparts (Figure 10). This is illustrated in Figure 14 for both cell lines.

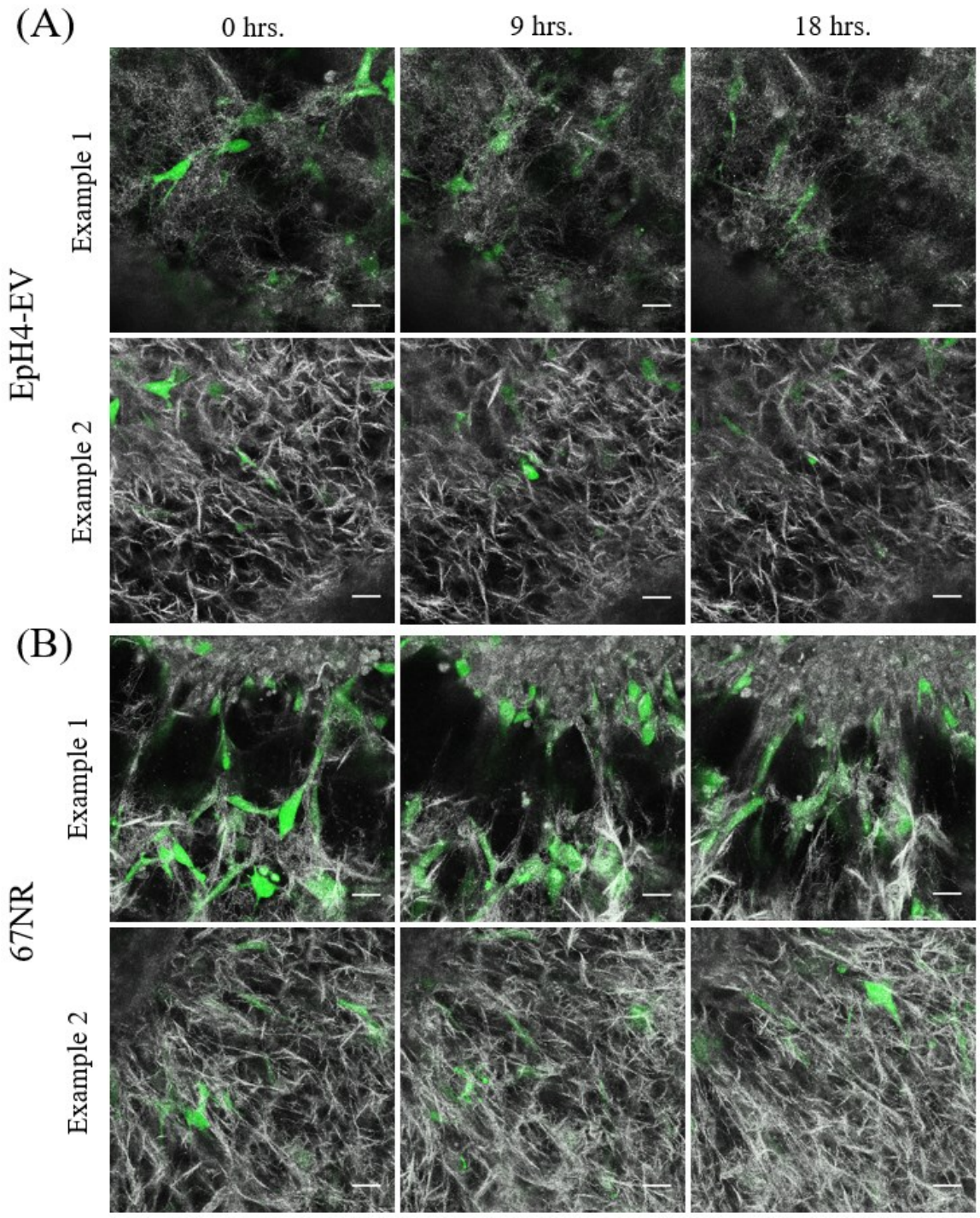

Figure 14. Reflectance and GFP (green) co-culture images of **(A)** EpH4-EV and **(B)** 67NR. For **(A)**, both examples exhibit some contractile properties, but have very little ECM remodeling. For **(B)** Example 1, individual 67NR cells tether onto the surrounding collagen and contract to form collagen networks that connect to the spheroid. For

Example 2, the 67NR spheroid significantly contracts to the point that the spheroid goes out of the frame during the imaging period. Both 67NR examples demonstrate significant ECM remodeling. Scale bar is for 100 μm.

Compared to Figure 6 and Figure 8(A), EpH4-EV in Figure 14 exhibits slightly more ECM remodeling. This can likely be attributed to the contractile, ECM-remodeling behaviors exhibited by fibroblasts as they randomly migrate throughout the collagen matrix[17]. For 67NR, however, there appears to be interactions between the spheroid and its surrounding fibroblasts as ECM remodeling significantly increases over time (Figure 14(B)). This is further evident when imaging the entire spheroid over time as shown in Figure 15.

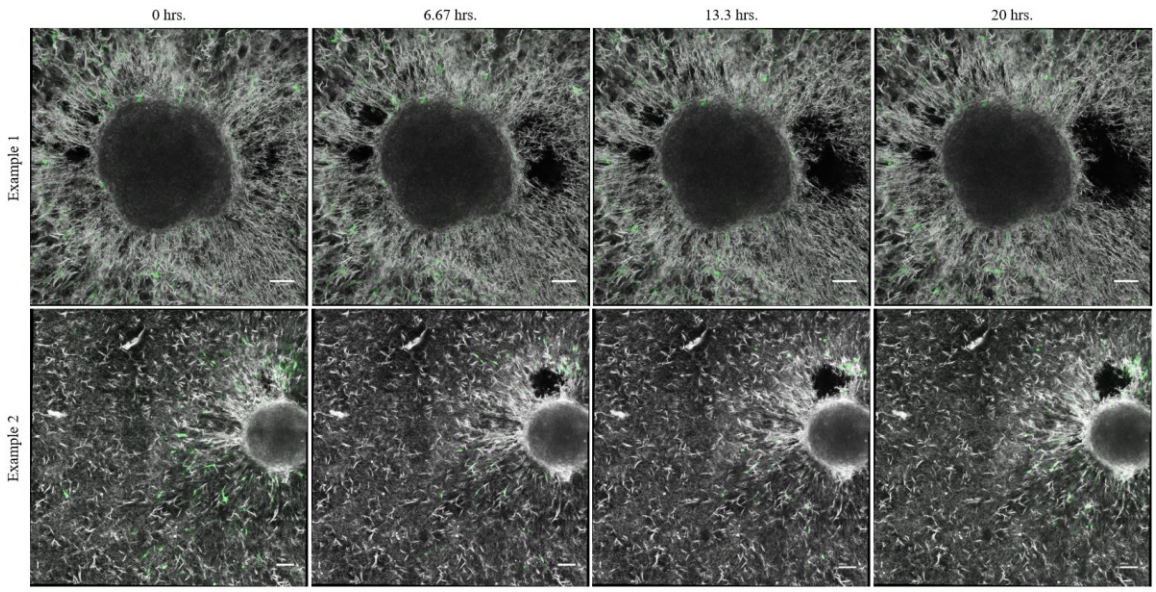

Figure 15. Entire co-cultured 67NR spheroid with reflectance and GFP (green) imaging. These examples show significant ECM remodeling that involves bulk spheroid contraction, radial collagen alignment, and pore generation. Scale bar is for 100 μm.

Over time, 67NR spheroids exhibit bulk spheroid contraction. Due to this, the surrounding collagen becomes radially aligned to the spheroid. The distance that this mechanical remodeling has on the collagen extends approximately 200-250 μm from the spheroid boundary. Moreover, along with the radially aligned collagen, large collagen pores are generated. These findings are quantified in Figure 16.

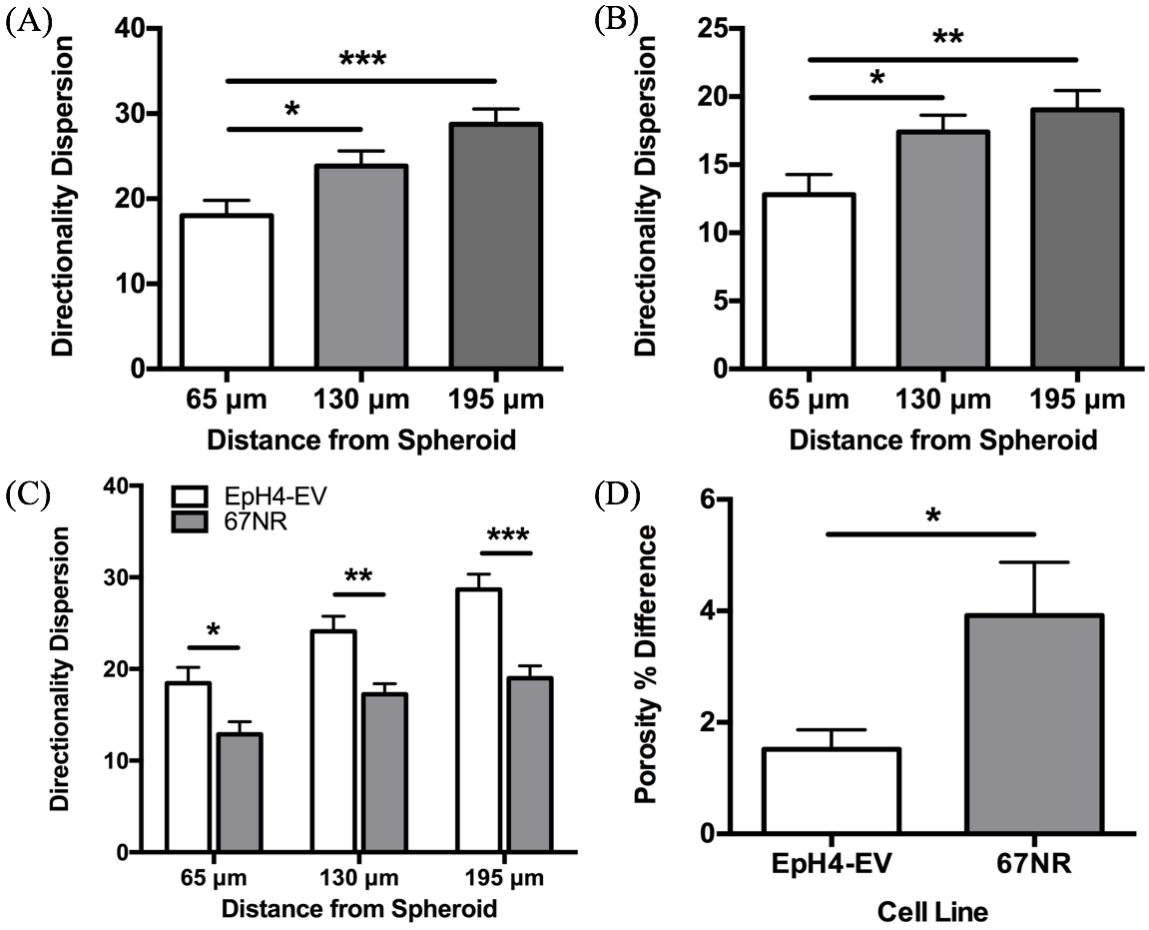

Figure 16. Directionality and porosity analysis of co-culture samples. Directionality dispersion as a function of distance of **(A)** EpH4-EV, **(B)** 67NR, **(C)** EpH4-EV vs 67NR. **(D)** Porosity between EpH4-EV and 67NR. Higher collagen alignment and pore generation in 67NR spheroids is observed. Compared to non-co-cultured samples, collagen alignment and pore generation for both cells lines in co-cultured samples increased. *p-value < 0.05, **p-value < 0.01, and ***p-value < 0.001. N = 5.

The results from Figure 16 correspond to the images in Figure 14 and 15. For EpH4-EV spheroids, the directionality dispersion is 18.0 ± 1.78, 23.8 ± 1.73, and 28.8 ± 1.77 for 65, 130, and 195 μm distances, respectively. Compared to Figure 9(A), the remodeling of EpH4-EV spheroids in co-culture is noticeably enhanced. For 67NR spheroids, the directionality dispersion is 12.8 ± 1.45, 17.4 ± 1.19, and 19.0 ± 1.4 for 65, 130, and 195 μm distances, respectively. These dispersions further support the mechanical force distance (200-250 μm) that 67NR spheroids have on the collagen as radial alignment is largely maintained over the distances measured. When comparing the two cell lines in Figure 16(C), it is clear that 67NR more significantly and aggressively remodels its TME through mechanical mechanisms over the distances measured. To further this point, pore generation is also greater in 67NR (3.92 ± 0.895) than in EpH4-EV (1.52 ± 0.325). This pore generation by 67NR is especially clear in Figure 15. Additionally, with the TFM data in Figure 13, it is understandable as to why 67NR is able to remodel its collagen in such an effective way.

Beyond collagen realignment and porosity, an interesting finding is the morphology difference between the two spheroids after 4 days of incubation. This is shown in Figure 17.

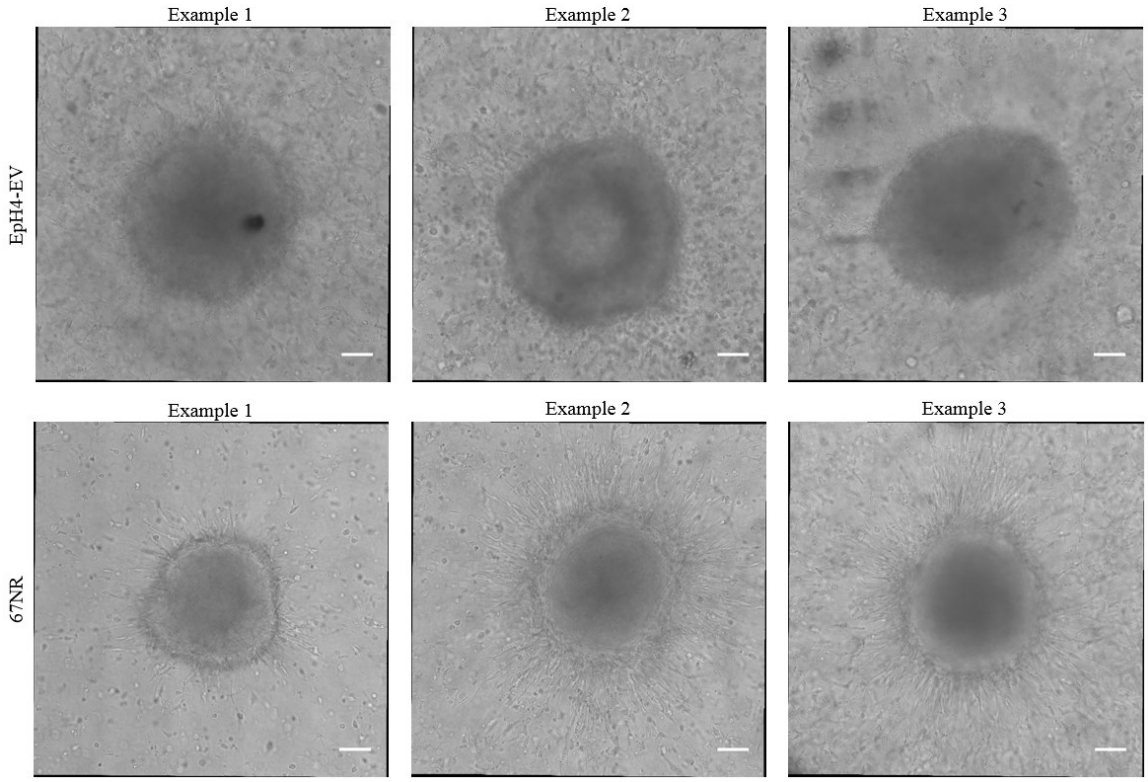

Figure 17. PMT transmitted light images comparing EpH4-EV and 67NR spheroid boundary. 67NR spheroids exhibited spindle-like morphology when co-cultured with fibroblasts. Scale bar is for 100 μm.

For co-culture samples, 67NR exhibits its characteristic spindle-like morphology that is seen when 2D culturing the cells. In 2D cultures, 67NR has a similar morphology to fibroblasts, whereas EpH4-EV and other epithelial cell lines typically have a circular morphology. This is not seen in samples without co-culture (Figure 9(B)), indicating some degree of communication via mechanical and/or chemical cues between the early-stage cancer spheroid and its surrounding fibroblasts. This could be due to NF to CAF transformation in the surrounding TME, where CAFs release cytokines and growth factors that change the spheroid's morphology. Despite that the underlying mechanism is

yet to be identified, it is confirmed that co-culturing in 67NR samples amplifies the spheroid's mechanical force generation and collagen remodeling properties.

Since 67NR is non-metastatic, the cells extending out to form this spindle-like morphology still remain attached to the spheroid and do not migrate as individual cells. Even for non-co-culture samples, individual cells did not migrate away from the spheroid. In comparison, some EpH4-EV spheroids have individual cells migrate out from the spheroid. This is interesting since EpH4-EV can form spheroids much more rapidly than 67NR. However, 67NR spheroids stay compact, and individual cells do not migrate out from the spheroids. This could likely be due to differences in E-cadherin and N-cadherin expression between the cell lines[6,53].

Fibroblast Migration Towards 67NR Spheroids

As mentioned earlier, tumor models typically show CAFs leading metastasizing cancer cells away from the tumor[28,29]. Throughout the imaging sessions, it is visualized and reported that fibroblasts exhibit preferential movement towards spheroids during early-stage (67NR) breast carcinoma while the control (EpH4-EV) had random fibroblast movement.

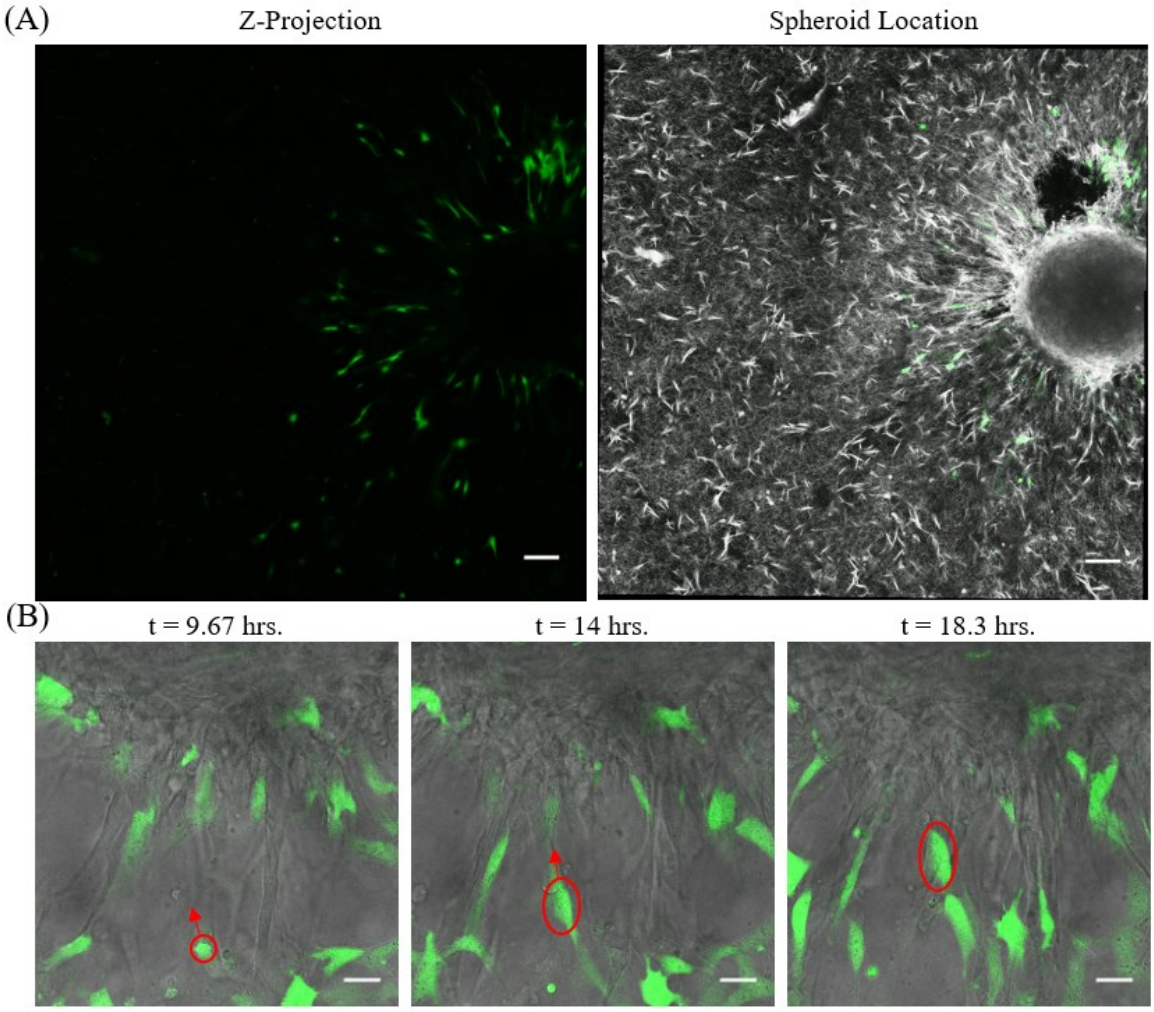

Figure 18. Fibroblast movement towards 67NR spheroids. **(A)** Z-projection and spheroid location reference showing general directional movement towards spheroid. Scale bar is for 100 μm. **(B)** Highlighted fibroblast shows movement towards spheroid over time. Scale bar is for 25 μm.

Here, we show GFP-3T3 fibroblast movement towards the spheroid over time. The z-projection (Figure 18(A)) shows general directionality towards the spheroid. Additionally, tracking individual fibroblasts over time further supports this claim (Figure 18(B)). This behavior can largely be contributed due to the mechanical remodeling done

by the 67NR spheroids. The radially aligned collagen forms a collagen track for easier, directed migration of fibroblasts towards the spheroids. This is clearly seen in Figure 18(A) as fibroblasts have a spindle-like morphology along the radially aligned collagen. We believe that this directional movement may be due to CAF formation that is aiding in cancer progression. However, further analysis, through mass spectrometry, needs to be conducted to show that this is indeed happening.

Future Directions

For this study, the next step is to perform mass spectrometry (mass spec.) on sectioned formalin-fixed, paraffin-embedded tissue (FFPET) and cryopreserved collagen samples. The method of mass spec. to be utilized is Time-of-Flight Secondary Ion Mass Spectrometry (ToF-SIMS) since this technique will give spatial information in the prepared collagen samples. This will quantify CAF markers, exosomes, etc. as a function of distance between the control (EpH4-EV) and early-stage (67NR) spheroid samples. In addition, the media from all samples will be put through mass spec. to identify and quantify cytokines (particularly TGF- β) and exosomes expression in the media. If these methods fail, then staining of the samples for CAF markers (αSMA, vimentin, tenascin-C, etc.) will be employed. Moreover, siRNA knockdown of Myosin II will be employed to inhibit the mechanical remodeling ability of the early-stage spheroid samples. This will help determine the effect that mechanical forces have on the transformation of NFs to CAFs. Besides these experiments, previous experiments such as TFM and FRAP will be repeated to obtain more data. Additionally, a MATLAB code for FRAP will be written specifically for rectangular FRAP to generate a more accurate fit for the recovery curve

as the current curve fitting method is generalized for all ROIs. Finally, with all of this data, the final step would be to write a manuscript for publication.

For future projects, this platform could be utilized in a plethora of other epithelial cancer cells lines of increasing malignancy. Moreover, this could even be employed on the 4T1-derived cell lines, which includes 67NR. It would be valuable to assess the varying degrees of remodeling of all stages of cancer progression in these cell lines. Additionally, studies showing why 67NR (and not EpH4-EV) is capable of generating such traction stresses and why fibroblasts migrate towards spheroids in early-stage cancer are of interest.

Conclusion

In this study, we show that early-stage cancer utilizes mechanical forces to effectively remodel its TME and promote cancer progression. Remodeling is done by realigning collagen into radial alignment and pore generation. These results are significant as 67NR is much more effective at ECM remodeling than EpH4-EV in non-co-culture samples. Moreover, due to this radial alignment, there is indeed a diffusion anisotropy that arises. This anisotropy should allow for the directed diffusion of cytokines and exosomes from the spheroid along a concentration gradient away from the spheroid towards NFs to convert them to CAFs. Future experiments should help support this claim. Furthermore, this remodeling behavior is attributed to mechanical force generation as TFM experiments show traction stress generation in 67NR spheroids while EpH4-EV spheroids exhibited little to none.

With co-culture experiments, 67NR's ECM remodeling ability in both collagen realignment and pore generation is amplified. Additionally, it is seen that this remodeling extends approximately 200-250 μm out from the spheroid boundary. Data support the lower limit of this claim as 67NR spheroids consistently realign collagen at the distances measured for this study. Moreover, 67NR spheroids exhibit characteristic spindle-like morphology when co-cultured. This co-culturing likely enhances the remodeling behavior as fibroblasts are most likely being converted into CAFs in these samples. Finally, we observed that fibroblast movement is random in EpH4-EV, but has directional migration towards the 67NR spheroids. With all of this in mind, future experiments will quantify CAF markers and exosomes, therefore giving support to claims associated with CAF development during 67NR co-culture samples. Moreover, future experiments will help determine how significant mechanical forces are in facilitating NF to CAF conversion.

References

1. S Siegel, R. L., Miller, K. D., & Jemal, A. (2017). Cancer statistics, 2017. CA: A Cancer Journal for Clinicians, 67(1), 7–30. http://doi.org/10.3322/caac.21387
2. Boyd, N. F., Dite, G. S., Stone, J., Gunasekara, A., English, D. R., McCredie, M. R. E., … Hopper, J. L. (2002). Heritability of Mammographic Density, a Risk Factor for Breast Cancer. *New England Journal of Medicine*, *347*(12), 886–894. http://doi.org/10.1056/NEJMoa013390
3. Alowami, S., Troup, S., Al-Haddad, S., Kirkpatrick, I., & Watson, P. H. (2003). Mammographic density is related to stroma and stromal proteoglycan expression. *Breast Cancer Research*, *5*(5), R129. http://doi.org/10.1186/bcr622
4. Schedin, P., & Keely, P. J. (2011). Mammary gland ECM remodeling, stiffness, and mechanosignaling in normal development and tumor progression. *Cold Spring Harbor Perspectives in Biology*, *3*(1), a003228. http://doi.org/10.1101/cshperspect.a003228
5. Oskarsson, T. (2013). Extracellular matrix components in breast cancer progression and metastasis. *The Breast*, *22*, S66–S72. http://doi.org/10.1016/J.BREAST.2013.07.012
6. Nelson- Piotrowski-Daspit, A. S., Nerger, B. A., Wolf, A. E., Sundaresan, S., & Nelson, C. M. (2017). Dynamics of Tissue-Induced Alignment of Fibrous Extracellular Matrix. *Biophysical Journal*, *113*(3), 702–713. http://doi.org/10.1016/j.bpj.2017.06.046
7. Provenzano BMC - Provenzano, P. P., Eliceiri, K. W., Campbell, J. M., Inman, D. R., White, J. G., & Keely, P. J. (2006). Collagen reorganization at the tumor-

stromal interface facilitates local invasion. *BMC Medicine*, *4*(1), 38. http://doi.org/10.1186/1741-7015-4-38

8. Riching, K. M., Cox, B. L., Salick, M. R., Pehlke, C., Riching, A. S., Ponik, S. M., … Keely, P. J. (2014). 3D collagen alignment limits protrusions to enhance breast cancer cell persistence. *Biophysical Journal*, *107*(11), 2546–58. http://doi.org/10.1016/j.bpj.2014.10.035
9. Cox, T. R., & Erler, J. T. (2011). Remodeling and homeostasis of the extracellular matrix: implications for fibrotic diseases and cancer. *Disease Models & Mechanisms*, *4*(2), 165–178. https://doi.org/10.1242/dmm.004077
10. Khaled, W., Reichling, S., Bruhns, O. T., Boese, H., Baumann, M., Monkman, G., … Ermert, H. (2004). Palpation imaging using a haptic system for virtual reality applications in medicine. *Studies in Health Technology and Informatics*, *98*, 147–53. Retrieved from http://www.ncbi.nlm.nih.gov/pubmed/15544261
11. Provenzano, P. P., Inman, D. R., Eliceiri, K. W., & Keely, P. J. (2009). Matrix density-induced mechanoregulation of breast cell phenotype, signaling and gene expression through a FAK-ERK linkage. *Oncogene*, *28*(49), 4326–43. http://doi.org/10.1038/onc.2009.299
12. Bissell - Rønnov-Jessen, L., Petersen, O. W., & Bissell, M. J. (1996). Cellular changes involved in conversion of normal to malignant breast: importance of the stromal reaction. *Physiological Reviews*, *76*(1), 69–125. http://doi.org/10.1152/physrev.1996.76.1.69
13. Kalluri, R. (2016). The biology and function of fibroblasts in cancer. *Nature Reviews Cancer*, *16*(9), 582–598. http://doi.org/10.1038/nrc.2016.73

14. Webber, J., Steadman, R., Mason, M. D., Tabi, Z., & Clayton, A. (2010). Cancer exosomes trigger fibroblast to myofibroblast differentiation. *Cancer Research*, *70*(23), 9621–30. http://doi.org/10.1158/0008-5472.CAN-10-1722

15. Hinz, B., Celetta, G., Tomasek, J. J., Gabbiani, G., & Chaponnier, C. (2001). Alpha-smooth muscle actin expression upregulates fibroblast contractile activity. *Molecular Biology of the Cell*, *12*(9), 2730–41. Retrieved from http://www.ncbi.nlm.nih.gov/pubmed/11553712

16. Phan, S. H. (2008). Biology of fibroblasts and myofibroblasts. *Proceedings of the American Thoracic Society*, *5*(3), 334–7. http://doi.org/10.1513/pats.200708-146DR

17. Montesano, R., & Orci, L. (1988). Transforming growth factor beta stimulates collagen-matrix contraction by fibroblasts: implications for wound healing. *Proceedings of the National Academy of Sciences of the United States of America*, *85*(13), 4894–7. Retrieved from http://www.ncbi.nlm.nih.gov/pubmed/3164478

18. Grinnell, F. (2000). Fibroblast–collagen-matrix contraction: growth-factor signalling and mechanical loading. *Trends in Cell Biology*, *10*(9), 362–365. http://doi.org/10.1016/S0962-8924(00)01802-X

19. Darby, I. A., Laverdet, B., Bonté, F., & Desmoulière, A. (2014). Fibroblasts and myofibroblasts in wound healing. *Clinical, Cosmetic and Investigational Dermatology*, *7*, 301–11. http://doi.org/10.2147/CCID.S50046

20. Dvorak - Flier, J. S., Underhill, L. H., & Dvorak, H. F. (1986). Tumors: Wounds That Do Not Heal. *New England Journal of Medicine*, *315*(26), 1650–1659. http://doi.org/10.1056/NEJM198612253152606

21. Dumont, N., Liu, B., Defilippis, R. A., Chang, H., Rabban, J. T., Karnezis, A. N., … Tlsty, T. D. (2013). Breast fibroblasts modulate early dissemination, tumorigenesis, and metastasis through alteration of extracellular matrix characteristics. *Neoplasia (New York, N.Y.)*, *15*(3), 249–62. Retrieved from http://www.ncbi.nlm.nih.gov/pubmed/23479504

22. Löhr, M., Schmidt, C., Ringel, J., Kluth, M., Müller, P., Nizze, H., & Jesnowski, R. (2001). Transforming growth factor-beta1 induces desmoplasia in an experimental model of human pancreatic carcinoma. *Cancer Research*, *61*(2), 550–5. Retrieved from http://www.ncbi.nlm.nih.gov/pubmed/11212248

23. Aoyagi, Y., Oda, T., Kinoshita, T., Nakahashi, C., Hasebe, T., Ohkohchi, N., & Ochiai, A. (2004). Overexpression of TGF-β by infiltrated granulocytes correlates with the expression of collagen mRNA in pancreatic cancer. *British Journal of Cancer*, *91*(7), 1316–1326. http://doi.org/10.1038/sj.bjc.6602141

24. Azmi, A. S., Bao, B., & Sarkar, F. H. (2013). Exosomes in cancer development, metastasis, and drug resistance: a comprehensive review. *Cancer Metastasis Reviews*, *32*(3–4), 623–42. http://doi.org/10.1007/s10555-013-9441-9

25. Hu, M., Yao, J., Cai, L., Bachman, K. E., van den Brûle, F., Velculescu, V., & Polyak, K. (2005). Distinct epigenetic changes in the stromal cells of breast cancers. *Nature Genetics*, *37*(8), 899–905. http://doi.org/10.1038/ng1596

26. Zeisberg, E. M., & Zeisberg, M. (2013). The role of promoter hypermethylation in fibroblast activation and fibrogenesis. *The Journal of Pathology*, *229*(2), 264–273. http://doi.org/10.1002/path.4120

27. Borges, F. T., Melo, S. A., Özdemir, B. C., Kato, N., Revuelta, I., Miller, C. A., … Kalluri, R. (2013). TGF-β1-containing exosomes from injured epithelial cells activate fibroblasts to initiate tissue regenerative responses and fibrosis. *Journal of the American Society of Nephrology : JASN*, *24*(3), 385–92. http://doi.org/10.1681/ASN.2012101031

28. Karagiannis, G. S., Poutahidis, T., Erdman, S. E., Kirsch, R., Riddell, R. H., & Diamandis, E. P. (2012). Cancer-associated fibroblasts drive the progression of metastasis through both paracrine and mechanical pressure on cancer tissue. *Molecular Cancer Research : MCR*, *10*(11), 1403–18. http://doi.org/10.1158/1541-7786.MCR-12-0307

29. Petrie, R. J., & Yamada, K. M. (2015). Fibroblasts Lead the Way: A Unified View of 3D Cell Motility. *Trends in Cell Biology*, *25*(11), 666–74. http://doi.org/10.1016/j.tcb.2015.07.013

30. Netti, P. A., Baxter, L. T., Boucher, Y., Skalak, R., & Jain, R. K. (1995). Time-dependent behavior of interstitial fluid pressure in solid tumors: implications for drug delivery. *Cancer Research*, *55*(22), 5451–8. Retrieved from http://www.ncbi.nlm.nih.gov/pubmed/7585615

31. Katt, M. E., Placone, A. L., Wong, A. D., Xu, Z. S., & Searson, P. C. (2016). In Vitro Tumor Models: Advantages, Disadvantages, Variables, and Selecting the Right Platform. *Frontiers in Bioengineering and Biotechnology*, *4*, 12. http://doi.org/10.3389/fbioe.2016.00012

32. Xu, X., Farach-Carson, M. C., & Jia, X. (2014). Three-dimensional in vitro tumor models for cancer research and drug evaluation. *Biotechnology Advances*, *32*(7), 1256–1268. http://doi.org/10.1016/j.biotechadv.2014.07.009

33. Justice, B. A., Badr, N. A., & Felder, R. A. (2009). 3D cell culture opens new dimensions in cell-based assays. *Drug Discovery Today*, *14*(1–2), 102–107. http://doi.org/10.1016/J.DRUDIS.2008.11.006

34. Edmondson, R., Broglie, J. J., Adcock, A. F., & Yang, L. (2014). Three-dimensional cell culture systems and their applications in drug discovery and cell-based biosensors. *Assay and Drug Development Technologies*, *12*(4), 207–18. http://doi.org/10.1089/adt.2014.573

35. Riedl, A., Schlederer, M., Pudelko, K., Stadler, M., Walter, S., Unterleuthner, D., … Dolznig, H. (2017). Comparison of cancer cells in 2D vs 3D culture reveals differences in AKT-mTOR-S6K signaling and drug responses. *Journal of Cell Science*, *130*(1), 203–218. http://doi.org/10.1242/jcs.188102

36. Adcock, A. F., Trivedi, G., Edmondson, R., Spearman, C., & Yang, L. (2015). Three-Dimensional (3D) Cell Cultures in Cell-based Assays for in-vitro Evaluation of Anticancer Drugs. *Journal of Analytical & Bioanalytical Techniques*, *6*(3). http://doi.org/10.4172/2155-9872.1000249

37. Discher, D. E., Janmey, P., & Wang, Y.-L. (n.d.). Tissue Cells Feel and Respond to the Stiffness of Their Substrate. Retrieved from http://www.seas.upenn.edu/~discher/pdfs/Cell_on_Gel-ScienceReview.pdf

38. Carisey, A., Stroud, M., Tsang, R., & Ballestrem, C. (2011). Fluorescence Recovery After Photobleaching (pp. 387–402). Humana Press. http://doi.org/10.1007/978-1-61779-207-6_26

39. Meyvis, T. K. L., De Smedt, S. C., Van Oostveldt, P., & Demeester, J. (1999). Fluorescence Recovery After Photobleaching: A Versatile Tool for Mobility and Interaction Measurements in Pharmaceutical Research. *Pharmaceutical Research*, *16*(8), 1153–1162. http://doi.org/10.1023/A:1011924909138

40. Ishikawa-Ankerhold, H. C., Ankerhold, R., & Drummen, G. P. C. (2012). Advanced Fluorescence Microscopy Techniques—FRAP, FLIP, FLAP, FRET and FLIM. *Molecules*, *17*(4), 4047–4132. http://doi.org/10.3390/molecules17044047

41. Leica. (n.d.). Single exponential function with one term. Retrieved from https://outlook.office.com/owa/?realm=jh.edu&path=/attachmentlightbox

42. Ellenberg, J., Siggia, E. D., Moreira, J. E., Smith, C. L., Presley, J. F., Worman, H. J., & Lippincott-Schwartz, J. (1997). Nuclear membrane dynamics and reassembly in living cells: targeting of an inner nuclear membrane protein in interphase and mitosis. *The Journal of Cell Biology*, *138*(6), 1193–206. http://doi.org/10.1083/JCB.138.6.1193

43. Soumpasis, D. M. (n.d.). THEORETICAL ANALYSIS OF FLUORESCENCE PHOTOBLEACHING RECOVERY EXPERIMENTS. Retrieved from https://www.ncbi.nlm.nih.gov/pmc/articles/PMC1329018/pdf/biophysj00223-0097.pdf

44. Deschout, H., Hagman, J., Fransson, S., Jonasson, J., Rudemo, M., Lorén, N., & Braeckmans, K. (2010). Straightforward FRAP for quantitative diffusion measurements with a laser scanning microscope. *Optics Express*, *18*(22), 22886. http://doi.org/10.1364/OE.18.022886

45. Wang, J. H.-C., & Lin, J.-S. (2007). Cell traction force and measurement methods. *Biomechanics and Modeling in Mechanobiology*, *6*(6), 361–371. http://doi.org/10.1007/s10237-006-0068-4

46. Tseng, Q., Duchemin-Pelletier, E., Deshiere, A., Balland, M., Guillou, H., Filhol, O., & Théry, M. (2012). Spatial organization of the extracellular matrix regulates cell-cell junction positioning. *Proceedings of the National Academy of Sciences of the United States of America*, *109*(5), 1506–11. http://doi.org/10.1073/pnas.1106377109

47. Tseng, Q. Traction Force Microscopy.

48. CJ - Aslakson, C. J., & Miller, F. R. (1992). Selective events in the metastatic process defined by analysis of the sequential dissemination of subpopulations of a mouse mammary tumor. *Cancer Research*, *52*(6), 1399–405. Retrieved from http://www.ncbi.nlm.nih.gov/pubmed/1540948

49. Avgustinova, A. *et al.* Tumour cell-derived Wnt7a recruits and activates fibroblasts to promote tumour aggressiveness. *Nat. Commun.* **7,** 10305 (2016).

50. Bolm, L. *et al.* The Role of Fibroblasts in Pancreatic Cancer: Extracellular Matrix Versus Paracrine Factors. *Transl. Oncol.* **10,** 578 (2017).

51. TdB Consultancy. (n.d.). FITC-dextran.

52. Style, R. W., Hyland, C., Boltyanskiy, R., Wettlaufer, J. S., & Dufresne, E. R. (2013). Surface tension and contact with soft elastic solids. *Nature Communications*, *4*, 2728. http://doi.org/10.1038/ncomms3728

53. Tao, K., Fang, M., Alroy, J., & Sahagian, G. G. (2008). Imagable 4T1 model for the study of late stage breast cancer. *BMC Cancer*, *8*, 228. http://doi.org/10.1186/1471-2407-8-228

54. Lou, Y., Preobrazhenska, O., auf dem Keller, U., Sutcliffe, M., Barclay, L., McDonald, P. C., … Dedhar, S. (2008). Epithelial-mesenchymal transition (EMT) is not sufficient for spontaneous murine breast cancer metastasis. *Developmental Dynamics*, *237*(10), 2755–2768. http://doi.org/10.1002/dvdy.21658

55. Stylianopoulos, T., Diop-Frimpong, B., Munn, L. L., & Jain, R. K. (2010). Diffusion Anisotropy in Collagen Gels and Tumors: The Effect of Fiber Network Orientation. *Biophysical Journal*, *99*(10), 3119–3128. http://doi.org/10.1016/j.bpj.2010.08.065

Curriculum Vitae

Education

The Johns Hopkins University Baltimore, MD
Master of Science and Engineering in Biomedical Engineering Expected May 2018

The University of Alabama Tuscaloosa, AL
Bachelor of Science in Chemical Engineering, *summa cum laude* May 2016

Research Experience

The Johns Hopkins University, MAFIA Lab Baltimore, MD
Graduate Research Assistant January 2017-Present

- Developing a 3D biomimetic platform to capture breast cancer's mechanical remodeling of its microenvironment in real-time via confocal microscopy.
- Computing and quantifying significant differences, such as collagen realignment, between breast carcinoma samples through image analysis techniques.
- Brainstorming and collaborating with colleagues to adjust experimental approaches; improve data and image analysis techniques, such as using MATLAB and incorporating additional ImageJ plugins; and explore potential research ideas.
- Assisting in the development and testing of an *in vitro* high-throughput screening device for drug safety that has obtained a provisional patent (co-inventor).

The University of Alabama, Integrative Animal Behavior Laboratory Tuscaloosa, AL
Undergraduate Research Assistant August 2013-April 2016

- Prepared and preserved Mangrove Rivulus samples via formalin-fixed paraffin-embedded tissue (FFPET) to investigate environmental epigenetics.
- Performed sectioning of over 100 tissue sample slides for imaging by using a microtome in an optimized manner.
- Executed hematoxylin and eosin (H&E) staining on tissue sample slides.
- Assisted in sacrificing samples for FFPET preservation.

Volunteering Experience

READ Alabama Tuscaloosa, AL
Student Facilitator, Mentor September-December 2012, February-April 2016

- Managed 3 mentors and 8 mentees by providing structure for mentor and mentee accountability.
- Increased 2 mentees' proficiency in reading and expanded their vocabulary by reading through assigned books, correcting the pronunciation of words, and defining unfamiliar words.

Al's Pals Mentorship Program Tuscaloosa, AL
Student Leader, Mentor September 2014-December 2015

- Recruited, interviewed, and evaluated prospective mentors for the program.
- Facilitated classroom activities for 8 mentors and 14 mentees by organizing discussions; maintaining a quiet, respectful environment; and resolving unnecessary behavior.
- Engaged mentees by devising additional mathematical problem sets for them to work on.

- Assisted 3 mentees in the understanding of their homework by explaining steps needed to arrive to the correct solution.

Alabama Action Tuscaloosa, AL
Student Leader, Volunteer August 2012-2015

- Renovated local, impoverished elementary schools through projects such as building a baseball field, beautifying a courtyard, and rebuilding a playground.
- Motivated students to pursue community service opportunities by recommending mentoring organizations.
- Delegated roles to 10 honors students in the renovation of a local elementary school.

Blue Med Africa Ho, Ghana
Medical Volunteer June 2014

- Supplied bandages and food, while also cleaning and rewrapping wounds, at a local village on a bi-weekly basis.
- Performed vitals, disinfected wounds, and provided dental and topical products at local schools and rural villages.

Children's Hospital Birmingham, AL
NICU Volunteer February-July 2013

- Managed the front desk to allow visitors visit the patients.
- Assisted nurses by watching over neonatal intensive care unit (NICU) patients.

International Service Learning Masaya, Nicaragua
Medical Volunteer March 2013

- Organized a local clinic for impoverished residents by announcing clinic dates to local residents and assisting in the set-up of the tables, stations, etc. for the clinic.
- Collaborated with 2 local doctors in Spanish to help diagnose and treat residents.

Presentations

- N. Yam, D. Maity, and Y. Chen. (2017) *Early-Stage Breast Cancer Spheroids Mechanically Remodel the Microenvironment More Significantly Compared to Their Normal and Metastatic Counterparts*. Microsymposium and Poster Presentation. 2017 ASCB|EMBO Meeting, Philadelphia, PA.

Campus Involvement

Omega Chi Epsilon Chemical Engineering Honors Society	April 2015-May 2016
Tau Beta Pi Engineering Honors Society	April 2014-May 2016
Delta Epsilon Iota Honors Society	October 2013-May 2016
Phi Eta Sigma Honors Society	April 2013-May 2016
Alpha Lambda Delta Honors Society	April 2013-May 2016